

Perturbative RGE systematics in precision observables

V. Bertone,^a G. Bozzi,^{b,c} F. Hautmann^{d,e}

^a*IRFU, CEA, Université Paris-Saclay, F-91191 Gif-sur-Yvette*

^b*Dipartimento di Fisica, Università di Cagliari, Cittadella Universitaria, I-09042 Monserrato*

^c*INFN, Sezione di Cagliari, Cittadella Universitaria, I-09042 Monserrato*

^d*Elementaire Deeltjes Fysica, Universiteit Antwerpen, B 2020 Antwerpen*

^e*Theoretical Physics Department, University of Oxford, Oxford OX1 3PU*

ABSTRACT: QCD calculations for collider physics make use of perturbative solutions of renormalisation group equations (RGEs). Ambiguities related to these solutions can contribute significantly to systematic uncertainties of theoretical predictions for physical observables. We propose a general method to estimate these systematic effects using techniques inspired by soft-gluon and transverse-momentum resummation approaches. We first discuss the cases of the evolution of strong coupling α_s , collinear parton-distribution functions (PDFs), and transverse-momentum-dependent distributions (TMDs). We then study the implications for precision observables in hadron-collider processes, such as the deep-inelastic scattering structure functions and the transverse-momentum distribution of the lepton pair in Drell-Yan production.

KEYWORDS: QCD, Resummation, Deep Inelastic Scattering, Drell-Yan Production

Contents

1	Introduction	1
2	Emergence of resummation scales	3
3	Strong coupling	6
4	Parton distribution functions	8
5	Transverse-momentum-dependent distributions	10
5.1	Evolution	11
5.2	Sudakov form factor	13
5.3	RGE systematics	14
5.4	Hysteresis and perturbative uncertainty on the Sudakov form factor	16
5.5	Matching on collinear distributions	19
6	Physical observables	22
6.1	Inclusive deep-inelastic electron-proton scattering	23
6.2	Transverse-momentum spectrum in Drell-Yan production	24
6.2.1	Large- q_T regime	24
6.2.2	Small- q_T regime	25
6.2.3	Matching small- q_T and large- q_T regions	25
7	Numerical applications	27
7.1	Deep-inelastic structure functions	27
7.2	Drell-Yan transverse momentum distribution	30
8	Conclusions	34
A	Collection of formulas	36
A.1	g -functions for the strong coupling	36
A.2	g -functions for PDFs	37
A.3	g functions for TMDs	38

1 Introduction

Many applications of Quantum Chromodynamics (QCD) to physics at high-energy colliders involve the solution of renormalisation group equations (RGEs). With the dramatic increase in precision of perturbative calculations for hard-scattering cross sections over the past few years, theoretical systematic uncertainties from RGE solutions become a potentially

important factor in determining the overall accuracy of theoretical predictions for collider processes.

In our recent work, Ref. [1], we studied these systematics in the case of QCD coupling α_s and collinear parton distribution functions (PDFs) [2–4], estimating the perturbative uncertainty associated with the solution of the corresponding RGEs. These effects were found to be non-negligible in kinematic regions which are phenomenologically important for PDF determinations from global fits to experimental data [5–11], as well as for extractions from future collider experiments [12–15]. As argued in Ref. [16], the fact that modern PDF fits do not account for these systematics is likely to lead to an underestimate of their uncertainties. Refs. [1, 17] illustrate this by studying the impact of RGE-related uncertainties on the deep-inelastic scattering (DIS) structure functions F_2 and F_L at next-to-leading order (NLO) and next-to-next-to-leading order (NNLO) accuracy in perturbative QCD. Further evidence is provided by the presence of logarithmically-enhanced higher-order contributions to the RGE kernels for PDF evolution at small values of Bjorken’s x_B [18–20] which are known to give rise to significant effects in F_2 . While these effects can be tamed by means of dedicated resummation techniques [20–31], a reliable estimate of RGE-related uncertainties is fundamental to assess the applicability region of fixed-order calculations. The relevance of such effects has also been noted in Refs. [32, 33] for analytic Sudakov resummation calculations, and in Ref. [34] for parton branching calculations.

In this paper, we provide more details to the analysis of the evolution of α_s and PDFs given in Ref. [1], and extend it to the evolution of transverse-momentum-dependent distributions (TMDs) [35–38]. We present a general framework aimed at evaluating theoretical systematic uncertainties related to the solution of RGEs on these quantities. We then study the impact of these effects on predictions for the inclusive neutral-current DIS structure functions (F_2 , F_L , and F_3) and for the transverse-momentum (q_T) distribution of the lepton pair in inclusive Drell-Yan (DY) production. The case of DIS is primarily relevant to current and forthcoming extractions of PDFs, and to precision QCD studies at future lepton-hadron experiments [13, 15, 39]. The case of DY is instead relevant to extractions of TMDs [40–46], as well as to precise determinations of the electroweak parameters of the Standard Model, such as the mass of the W boson [47, 48]. These studies often require the matching of the small- q_T calculation, which can be written in terms of TMDs, to the large- q_T calculation, which is instead expressed in terms of (collinear) PDFs [49–65]. We carry out the matching keeping track of the theoretical uncertainties stemming from both small- and large- q_T regimes, finally providing an estimate over the entire spectrum which consistently incorporates all uncertainties.

We organise the presentation of our study as follows. In Sec. 2, we discuss in general terms the emergence of RGE-related perturbative uncertainties and devise the strategy to estimate them by introducing the resummation scales. In Secs. 3 and 4, we examine the cases of the strong coupling and PDFs by reviewing and extending the results of Ref. [1]. In Sec. 5, we analyse the case of TMDs. We express their evolution in terms of a Sudakov form factor and present quantitative results on the associated RGE systematic uncertainties. In Sec. 6, we discuss uncertainty estimates for specific physical observables: the DIS structure functions and the transverse-momentum distribution of the lepton pair in DY production.

In Sec. 7, we perform numerical calculations for the neutral-current structure functions F_2 , F_L and F_3 , and for the DY differential cross $d\sigma/dq_T$, illustrating the corresponding RGE theoretical uncertainties in comparison with renormalisation- and factorisation-scale uncertainties. We give our conclusions in Sec. 8. The lengthy expressions for the g -functions that govern the evolution of the quantities considered in this paper, *i.e.*, α_s , PDFs, and TMDs, are collected in the App. A.

2 Emergence of resummation scales

In this section, we discuss in general terms how resummation scales emerge when solving RGEs whose anomalous dimensions are known to some fixed order in perturbation theory. To carry out this investigation, we start by considering RGEs of the general form

$$\frac{d}{d \ln \mu} \ln R(\mu) = \gamma(\alpha_s(\mu)), \quad (2.1)$$

where R is a renormalised quantity, function of the renormalisation scale μ , and γ is the appropriate anomalous dimension computable in perturbation theory as a power series in the coupling α_s . The perturbative expansion of the anomalous dimension γ truncated at order k is given by

$$\gamma(\alpha_s(\mu)) = \sum_{n=0}^k a_s^{n+1}(\mu) \gamma_n, \quad (2.2)$$

with $a_s(\mu) \equiv \alpha_s(\mu)/(4\pi)$. At any finite truncation order k , we analyse solutions of Eq. (2.1) obtained by methods which differ by subleading terms. Specifically, we adopt two different strategies. The first relies on solving Eq. (2.1) *analytically* by expressing the “evolved” quantity $R(\mu)$ in terms of the boundary condition $R(\mu_0)$ in a closed analytic form. The advantage of having an analytic, and thus numerically fast, implementation of the running comes with a drawback. As discussed in Ref. [1], analytic solutions beyond the leading-order approximation in Eq. (2.2) ($k > 0$) are derived by means of perturbative expansions that cause a violation of Eq. (2.1) by subleading terms with respect to the perturbative accuracy of the anomalous dimension. This drawback is amended by the second strategy which instead relies on *numerical* solutions of Eq. (2.1). Indeed, up to numerical inaccuracies, this approach guarantees by construction an exact equality between left-hand and right-hand sides of Eq. (2.1). The disadvantage is that numerical solutions are computationally more expensive than analytic ones.

To characterise the differences between analytic and numerical solutions, we introduce the evolution operator G which connects R at two scales μ and μ_0 :¹

$$R(\mu) = G(\mu, \mu_0)R(\mu_0). \quad (2.3)$$

We relate the differences between solutions to the fact that, due to subleading orders, one may have, for a given μ' , $G(\mu, \mu_0) \neq G(\mu, \mu')G(\mu', \mu_0)$. We refer to this as *perturbative hysteresis* [1].

¹The evolution operator G is in general a non-local and non-linear operator. Therefore, in this context G is to be regarded as a formal construction useful to introduce the concept of perturbative hysteresis and whose actual realisation is unimportant.

From this analysis, it emerges that analytic solutions are affected by perturbative hysteresis, while numerical solutions are not. However, we stress that the amount of perturbative hysteresis of a given solution is not a discriminant of its goodness. Indeed, analytic and numerical solutions based on an anomalous dimension truncated at the same order are all equally good from the viewpoint of perturbative accuracy. On the other hand, the very existence of perturbative hysteresis is a manifestation of a theoretical uncertainty that affects *any* solution of Eq. (2.1) with perturbatively computed anomalous dimension. The purpose of this work is to devise a strategy to estimate this uncertainty.

In the context of analytic solutions, this can be achieved using techniques borrowed from soft-gluon and transverse-momentum resummation [66–68]. Indeed, such solutions have the advantage of explicitly exposing terms proportional to $L_1 = a_s(\mu_0) \ln(\mu/\mu_0)$. Since μ_0 and μ are potentially far apart, L_1 can be large in spite of the presence of $a_s(\mu_0)$ and thus it cannot be treated as a perturbative parameter. This implies the need to sum powers of L_1 to all orders in perturbation theory. Once the analytic solution of the RGE has been obtained, one can decompose all instances of L_1 as follows,

$$L_1 = L_\kappa - a_s(\mu_0) \ln \kappa, \quad \text{with} \quad L_\kappa = a_s(\mu_0) \ln \left(\frac{\kappa\mu}{\mu_0} \right), \quad (2.4)$$

where the scale $\kappa\mu$ is dubbed *resummation scale*. Provided that κ is of order $\mathcal{O}(1)$, the second term in the decomposition of L_1 , *i.e.*, $a_s(\mu_0) \ln \kappa$, is perturbatively small. This allows one to expand the analytic solution of the RGE around $L_1 = L_\kappa$, retaining only terms within perturbative accuracy. The net result is an analytic solution that sums all powers of L_κ , while retaining powers of $a_s(\mu_0) \ln \kappa$ only up to the nominal accuracy. Variations of κ in the vicinity of $\kappa = 1$ generate subleading terms that provide an estimate of the perturbative uncertainty associated with the analytic solution of the RGE.

The observation that analytic solutions violate their RGEs by subleading terms suggests a way to assess perturbative uncertainties also in the context of numerical solutions. One could introduce arbitrary subleading corrections to the anomalous dimension γ and then solve the corresponding RGE numerically. Differences at the level of numerical solutions obtained with different subleading terms in the anomalous dimension would then provide an estimate of the perturbative uncertainty of the solution itself. A way to generate subleading corrections in fixed-order quantities is through scale variations. To be more specific, let us consider the anomalous dimension γ truncated at NLO accuracy,

$$\gamma = a_s(\mu)\gamma_0 + a_s^2(\mu)\gamma_1. \quad (2.5)$$

Then we use the expanded solution for the running of the strong coupling to express $a_s(\mu)$ in terms of $a_s(\xi\mu)$, where ξ is a parameter of order $\mathcal{O}(1)$,²

$$a_s(\mu) = a_s(\xi\mu) - a_s^2(\xi\mu)\beta_0 \ln \xi + \mathcal{O}(\alpha_s^3), \quad (2.7)$$

²The expansion in Eq. (2.7) comes from the solution to the RGE

$$\frac{d \ln a_s(\mu)}{d \ln \mu} = a_s(\mu)\beta_0 + \mathcal{O}(\alpha_s^2). \quad (2.6)$$

that plugged into Eq. (2.5) gives

$$\gamma = a_s(\xi\mu)\gamma_0 + a_s^2(\xi\mu) [\gamma_1 - \beta_0 \ln \xi] + \mathcal{O}(\alpha_s^3), \quad (2.8)$$

where subleading terms of order $\mathcal{O}(\alpha_s^3)$ have been neglected. From a perturbative perspective, solving Eq. (2.1) using the anomalous dimension in Eq. (2.5) or that in Eq. (2.8) is equivalent. However, the two solutions will be numerically different. As argued above, their difference can be interpreted as an estimate of the perturbative uncertainty associated to the solution of the RGE obtained with anomalous dimension truncated at NLO accuracy. Of course, this procedure can be extended to any finite truncation order. Therefore, variations of the parameter ξ in Eq. (2.8) when solving Eq. (2.1) numerically are analogous to variations of the parameter κ introduced in Eq. (2.4) when the solution is analytic. In this sense, also the scale $\xi\mu$ is a resummation scale. We will explicitly show below, considering the RGE of the strong coupling at NLO accuracy, that there is indeed a one-to-one correspondence between κ and ξ . Therefore, variations by the same amount of κ and ξ are expected to provide comparable estimates of the theoretical uncertainty on the analytic and numerical solutions of the RGE.

In the following, we will implement the strategy outlined above for the cases of strong coupling α_s , PDFs, and TMDs (Secs. 3, 4, and 5, respectively). In all cases, we will derive analytic solutions to the RGEs and compare them to the respective numerical solutions. In doing so, we will also vary the resummation-scale parameters κ and ξ and compare the resulting uncertainty bands. In the case of TMDs, we will show explicit results for the hysteresis produced by the analytic solution (corresponding results for α_s and PDFs can be found in Ref. [1]). On a case-by-case basis, we will also define the accuracy of the results. We will consider the *logarithmic accuracy* (leading-logarithm (LL), next-to-leading-logarithm (NLL), and so on, as opposed to fixed-order accuracy used for perturbative calculations truncated at some finite order in α_s) for “single-logarithmic” resummation, as in the cases of α_s and PDFs, and for “double-logarithmic” resummation, as in the case of TMDs.

After the discussion on the solution of RGEs, we will move to examining the implications of RGE systematic uncertainties on the perturbative computation of phenomenologically relevant physical observables (Secs. 6 and 7). The role of these uncertainties in single-logarithmic resummation will be studied in the cases of inclusive neutral-current DIS and large- q_T DY production. The case of double-logarithmic resummation will be studied by considering DY production at small q_T . In these studies, we will also investigate the interplay between RGE systematic uncertainties, parameterised by resummation scales, and the more common perturbative uncertainties obtained by variations of renormalisation and factorisation scales.

3 Strong coupling

We start our analysis by considering the evolution of the strong coupling α_s . In Eqs. (2.1) and (2.2), we set $R = a_s$ and $\gamma = \beta$, where β is the QCD β -function, and obtain³

$$\frac{d}{d \ln \mu} \ln a_s(\mu) = \beta(\alpha_s(\mu)) = \sum_{n=0}^k a_s^{n+1}(\mu) \beta_n. \quad (3.2)$$

Truncating the series at order k in Eq. (3.2), *i.e.*, using a N^k LO accurate β -function, produces solutions that are N^k LL accurate. The corresponding analytic solution can be written as [1]

$$a_s^{N^k \text{LL}}(\mu) = \sum_{l=0}^k a_s^{l+1}(\mu_0) g_{l+1}^{(\beta)}(\lambda, \kappa), \quad (3.3)$$

where we have defined

$$\lambda = a_s(\mu_0) \beta_0 \ln \left(\frac{\kappa \mu}{\mu_0} \right), \quad (3.4)$$

with the parameter κ introduced in Eq. (2.4), and the functions $g_i^{(\beta)}$ collected in App. A.1 up to $i = 4$, necessary to achieve N^3 LL accuracy. As explained above, variations of κ around $\kappa = 1$ by a moderate factor (typically of 2) allow one to estimate the perturbative uncertainty that affects the running of the coupling.

Alternatively, Eq. (3.2) can be solved numerically. As argued in Sec. 2, an estimate of the theoretical uncertainty associated to the numerical solution can be achieved by performing scale variations at the level of the β -function. Displacing the scale μ by a factor ξ in the r.h.s. of Eq. (3.2) with $k = 4$ and using the expanded evolution of α_s truncated at $\mathcal{O}(\alpha_s^4)$, we obtain

$$\begin{aligned} \beta(\alpha_s(\mu)) = & a_s(\xi\mu) \beta_0 \left[1 + a_s(\xi\mu) (b_1 - 2\beta_0 \ln \xi) + a_s^2(\xi\mu) \left(-5b_1\beta_0 \ln \xi + 3\beta_0^2 \ln^2 \xi + b_2 \right) \right. \\ & \left. + a_s^3(\xi\mu) \left(13b_1\beta_0^2 \ln^2 \xi - 3b_1^2\beta_0 \ln \xi - 6b_2\beta_0 \ln \xi - 4\beta_0^3 \ln^3 \xi + b_3 \right) \right] + \mathcal{O}(\alpha_s^5), \end{aligned} \quad (3.5)$$

where $b_n = \beta_n/\beta_0$. Eq. (3.5) defines a new β -function that differs from the original one by subleading corrections. This β -function can be used in numerical solutions to estimate the corresponding theoretical uncertainty by varying the parameter ξ .

An inconvenient feature of the β -function in Eq. (3.5) is that it relates the derivative of the strong coupling α_s computed at μ (l.h.s. of Eq. (3.2)) with α_s computed at $\xi\mu$. This gives rise to a “retarded” or an “advanced” differential equation whose solution is more complicated than that of a standard differential equation. To overcome this difficulty, one

³Note that often the β -function is defined through the equation (see *e.g.* Ref. [69])

$$\frac{d\alpha_s}{d \ln \mu^2} = -\alpha_s(\mu) \sum_{n=0}^k a_s^{n+1}(\mu) \beta_n. \quad (3.1)$$

Using this form, the anomalous dimension γ in Eq. (2.1) should be identified with $\gamma = -2\beta/a_s$.

can employ the analytic solution in Eq. (3.3) to express $a_s(\xi\mu)$ in terms of $a_s(\mu)$ so that, retaining only the relevant orders, one obtains

$$\begin{aligned}
\beta(\alpha_s(\mu)) = & a_s(\mu)\beta_0 \left[(g_1^{(\beta)})^2 + a_s(\mu) \left(b_1(g_1^{(\beta)})^3 + 2g_1^{(\beta)} \left(g_2^{(\beta)} - (g_1^{(\beta)})^2 \beta_0 \ln \xi \right) \right) \right. \\
& + a_s^2(\mu) \left(-5b_1(g_1^{(\beta)})^4 \beta_0 \ln \xi + b_2(g_1^{(\beta)})^4 + 3b_1 g_2^{(\beta)} (g_1^{(\beta)})^2 + 3(g_1^{(\beta)})^4 \beta_0^2 \ln^2 \xi \right. \\
& \quad \left. - 6g_2^{(\beta)} (g_1^{(\beta)})^2 \beta_0 \ln \xi + 2g_3^{(\beta)} g_1^{(\beta)} + (g_2^{(\beta)})^2 \right) \\
& + a_s^3(\mu) \left(13b_1(g_1^{(\beta)})^5 \beta_0^2 \ln^2 \xi - 3b_1^2(g_1^{(\beta)})^5 \beta_0 \ln \xi - 6b_2(g_1^{(\beta)})^5 \beta_0 \ln \xi \right. \\
& \quad - 20b_1 g_2^{(\beta)} (g_1^{(\beta)})^3 \beta_0 \ln \xi + b_3(g_1^{(\beta)})^5 + 4b_2 g_2^{(\beta)} (g_1^{(\beta)})^3 + 3b_1 g_3^{(\beta)} (g_1^{(\beta)})^2 \\
& \quad + 3b_1 (g_2^{(\beta)})^2 g_1^{(\beta)} - 4(g_1^{(\beta)})^5 \beta_0^3 \ln^3 \xi + 12g_2^{(\beta)} (g_1^{(\beta)})^3 \beta_0^2 \ln^2 \xi \\
& \quad \left. \left. - 6g_3^{(\beta)} (g_1^{(\beta)})^2 \beta_0 \ln \xi - 6(g_2^{(\beta)})^2 g_1^{(\beta)} \beta_0 \ln \xi + 2g_4^{(\beta)} g_1^{(\beta)} + 2g_2^{(\beta)} g_3^{(\beta)} \right) \right] + \mathcal{O}(\alpha_s^5), \tag{3.6}
\end{aligned}$$

where the $g^{(\beta)}$ -functions are to be computed at $\lambda_\xi = a_s(\mu)\beta_0 \ln \xi$ and $\kappa = 1$. We note that, setting $\xi = 1$ so that $\lambda_\xi = 0$, one finds that $g_1^{(\beta)} = 1$ while $g_i^{(\beta)} = 0$ for $i > 1$, which consistently reduces Eq. (3.6) to the usual β -function. Thus, Eq. (3.6) allows for estimates of theoretical uncertainties by variations of ξ , and produces a differential equation which can be solved by standard methods.

We now show explicitly that, at NLL accuracy, the analytic solution in Eq. (3.3) for a generic value of κ corresponds, up to subleading terms, to the numerical solution obtained using the β -function in Eq. (3.6) with $\xi = \kappa$. To do so, we observe that the NLL analytic solution obtained using Eq. (3.3) can be written as

$$a_s^{\text{NLL}}(\mu) = a_s^{\text{NLL}}(\kappa\mu, 1) - \left(a_s^{\text{LL}}(\kappa\mu, 1) \right)^2 \beta_0 \ln \kappa. \tag{3.7}$$

Taking the derivative with respect to $\ln \mu$, one gets

$$\frac{d \ln a_s^{\text{NLL}}(\mu, \kappa)}{d \ln \mu} = a_s^{\text{NLL}}(\kappa\mu, 1) \beta_0 + \left(a_s^{\text{LL}}(\kappa\mu, 1) \right)^2 \left[\beta_1 - 2(\beta_0)^2 \ln \kappa \right] + \mathcal{O}(\alpha_s^3), \tag{3.8}$$

which coincides with the r.h.s. of Eq. (3.6) truncated at $\mathcal{O}(\alpha_s^2)$ if one identifies κ with ξ . It can be shown by similar methods that the same equivalence between κ and ξ holds also at higher orders in perturbation theory.

We finally move to presenting quantitative results for the analytic and numerical evolutions of the strong coupling. Fig. 1 shows the running of α_s computed at NLL (top-left), NNLL (top-right), and N³LL (bottom) accuracies, over a wide range in energy, obtained using $\alpha_s(M_Z) = 0.118$ as a boundary condition. The upper panel of each plot displays the analytic (green) and the numerical (orange) runnings of α_s along with bands that respectively correspond to variations of κ and ξ in the range $[0.5 : 2]$. Lower panels show the same curves normalised to the central-value predictions obtained with $\kappa = \xi = 1$. In accordance with the correspondence between κ and ξ discussed above, we observe that the uncertainties on analytic and numerical solutions at any given order are generally comparable in size. We also see that the size of the bands shrinks as one moves from NLL to N³LL, as expected. In particular, we observe that at NNLL and N³LL uncertainties are

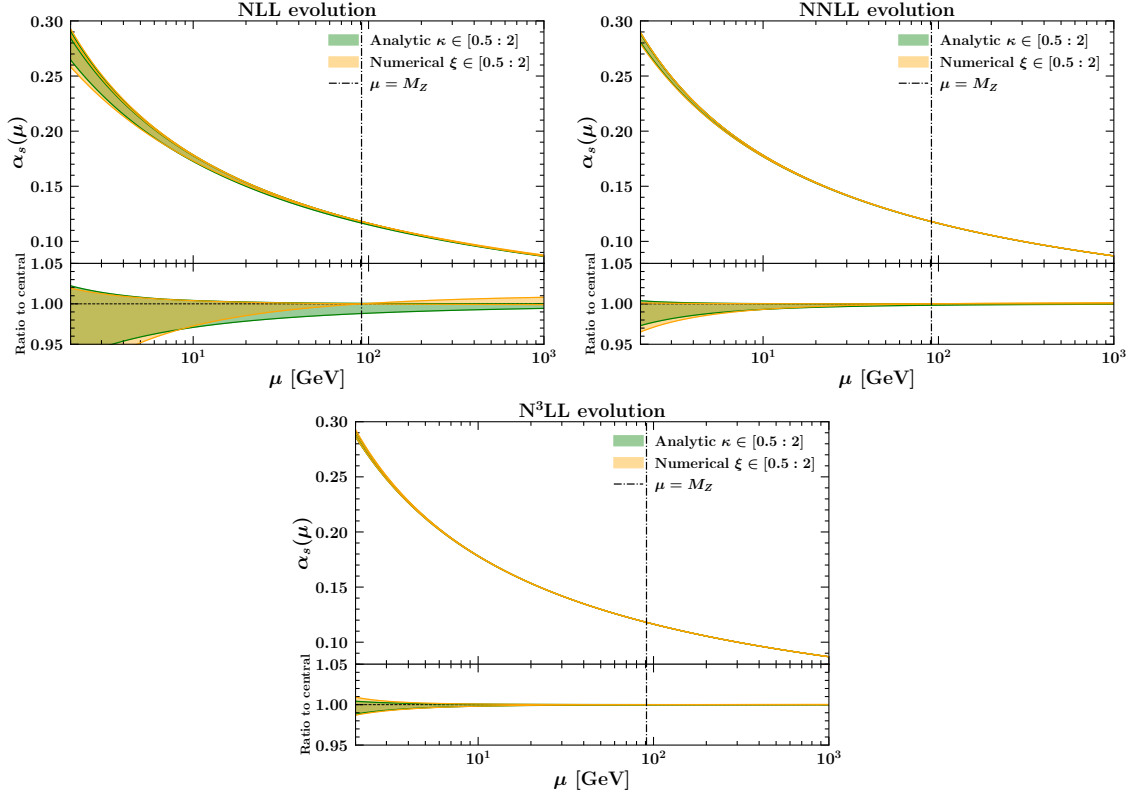


Figure 1. Analytic and numerical evolutions of the strong coupling α_s in the range $\mu \in [2 : 1000]$ GeV at NLL (top-left plot), NNLL (top-right plot), and N³LL (bottom plot) accuracies. The boundary condition is set at $\alpha_s(M_Z) = 0.118$. Uncertainty bands correspond to variations of the parameters κ and ξ for analytic and numerical solutions, respectively, in the ranges $\kappa, \xi \in [0.5 : 2]$. Lower panels display the bands normalised to the respective central-value curves obtained with $\kappa = \xi = 1$. The vertical dot-dashed line indicates the scale $\mu = M_Z$ where the boundary condition is set. At this scale the uncertainty on numerical solutions reduces to zero.

well below the 1% level for most of the values of μ considered. However, for scales of the order of 2 GeV, the NNLL bands reach the 3-4% level, while the N³LL ones remain at the 1% level. We note that the uncertainty on the numerical solution is zero at $\mu = M_Z$, due to the fact that this corresponds to the boundary-condition energy and thus no theoretical uncertainty related to the running is present here. However, this feature is not shared by the analytic solution.

4 Parton distribution functions

We next consider the case of Eq. (2.1) in which the quantity R is identified with a Mellin moment of a flavour non-singlet collinear PDF f , and γ is its anomalous dimension [2–

4, 70–73].⁴ The analytic solution takes the form [1]

$$f^{\text{N}^k\text{LL}}(\mu) = g_0^{(\gamma),\text{N}^k\text{LL}}(\lambda, \kappa) \exp \left[\sum_{l=0}^k a_s^l(\mu_0) g_{l+1}^{(\gamma)}(\lambda, \kappa) \right] f(\mu_0). \quad (4.1)$$

The $g^{(\gamma)}$ -functions depend on the variable λ defined in Eq. (3.4) and on the resummation scale parameter κ introduced in Eq. (2.4). In order to achieve N^kLL accuracy, one needs to truncate $g_0^{(\gamma),\text{N}^k\text{LL}}$ at $\mathcal{O}(\alpha_s^k)$ and include functions $g_i^{(\gamma)}$ in the exponential up to $i = k + 1$. App. A.2 collects these functions up to NNLL accuracy. The $g^{(\gamma)}$ -functions that enter the exponential in Eq. (4.1) are entirely defined in terms of the $g^{(\beta)}$ -functions responsible for the analytic evolution of α_s and of the LO coefficient of the PDF anomalous dimension γ_0 . Perturbative coefficients of the anomalous dimension beyond LO contribute to $g_0^{(\gamma),\text{N}^k\text{LL}}$ in such a way that coefficients up to γ_k are necessary to achieve N^kLL accuracy.

As in the case of the strong coupling, numerical solutions to the RGE for PDFs are obtained by displacing the argument of α_s in the expansion of the anomalous dimension by a factor of ξ , so that its variations can be used to estimate the theoretical systematic uncertainty. The resulting anomalous dimension valid up to NNLL accuracy reads

$$\begin{aligned} \gamma(\alpha_s(\mu)) &= a_s(\xi\mu)\gamma_0 + a_s^2(\xi\mu) [\gamma_1 - \beta_0\gamma_0 \ln \xi] \\ &+ a_s^3(\xi\mu) \left[\gamma_2 - (\beta_1\gamma_0 + 2\beta_0\gamma_1) \ln \xi + \beta_0^2\gamma_0 \ln^2 \xi \right] + \mathcal{O}(\alpha_s^4). \end{aligned} \quad (4.2)$$

Analogously to the running of α_s , one can show that variations of ξ in numerical solutions are in one-to-one correspondence with variations of κ in analytic solutions obtained through Eq. (4.1).

In view of the phenomenological assessment of theoretical uncertainties at the level of physical observables presented in Sec. 7, it is interesting to analytically study the behaviour of resummation-scale uncertainties on PDFs. To this purpose, let $f(\nu; \xi)$ be the PDF moment at the scale ν evolved from the scale ν_0 using ξ as resummation-scale parameter. Defining

$$\Delta f(\nu; \xi) = f(\nu; \xi) - f(\nu; 1), \quad (4.3)$$

and using Eq. (4.2) truncated at $\mathcal{O}(\alpha_s^2)$ so that the resulting evolution is NLL accurate, we find

$$\Delta f(\nu, \xi) = (a_s^2(\xi\nu) - a_s^2(\xi\nu_0)) \ln \xi \left(\gamma_1 + \frac{1}{2}b_1\gamma_0 - \frac{1}{2}\beta_0\gamma_0 \ln \xi \right) f(\nu; 1) + \mathcal{O}(\alpha_s^3). \quad (4.4)$$

A few comments are in order. First, we find $\Delta f \sim \mathcal{O}(\alpha_s^2)$, that is, a subleading effect at NLL accuracy, as expected. Second, $\Delta f \sim \ln \xi$, so that it approaches zero as $\xi \rightarrow 1$, again as expected. Finally, $\Delta f \sim a_s^2(\xi\nu) - a_s^2(\xi\nu_0)$, which has important consequences.⁵ If $\nu \simeq \nu_0$, no matter how small ν and thus how large $a_s(\xi\nu)$, Δf remains small. If,

⁴The discussion is generalisable to flavour-singlet distributions and x space, using anomalous dimension matrices and path-ordered exponentials where appropriate.

⁵In general, one can show that, at N^kLL , $\Delta f(\nu; \xi)$ is proportional to $a_s^{k+1}(\xi\nu) - a_s^{k+1}(\xi\nu_0)$.

instead, $\nu \gg \nu_0$ (or $\nu \ll \nu_0$), Δf will be dominated by the small scale, no matter how large the large scale is. This behaviour of resummation-scale variations is very specific and differs from that of usual renormalisation- and factorisation-scale variations. Indeed, let us assume that PDFs are measured (fitted) at the scale $\nu_0 \simeq 1$ GeV, as it is often the case. It follows that resummation-scale variations in the computation of a physical observable at the scale ν will tend to produce a small departure from the central scale when $\nu \simeq \nu_0$ and to grow as ν becomes large. This is opposite to the typical trend of renormalisation- and factorisation-scale variations, which are large at small ν and small at large ν . We will present quantitative evidence of this behaviour in Sec. 7.1 when studying DIS structure functions (see also Ref. [1]). We conclude that RGE solutions give rise to an additional source of theoretical uncertainties, which is not accounted for by variations of renormalisation and/or factorisation scales. Indeed, while the latter estimate uncertainties specific to the region of the hard-scattering scale ν , the former accounts for the “cumulative” uncertainty that stems from evolution between ν_0 and ν .

Finally, we present a numerical comparison between analytic and numerical PDF evolution using the settings of the benchmark exercise of Ref. [74]. To this purpose, we have used the public code MELA [75]. In Fig. 2, we show the total valence distribution $V = \sum_q (q - \bar{q})$ as a function of x evolved from $\nu_0 = \sqrt{2}$ GeV to $\nu = 100$ GeV at NLL (left) and NNLL (right). Each curve has an uncertainty band deriving from variations of the resummation-scale parameters κ and ξ in the analytic and numerical solutions, respectively. As usual, the upper panel of each plot shows the actual distributions along with their uncertainty bands, while the lower panel shows the ratio to the $\kappa = \xi = 1$ curves. As expected, we see that the size of the uncertainty bands is reduced as one moves from NLL to NNLL. In addition, at each of the two orders considered, analytic and numerical bands are comparable in size, showing again the correspondence between variations of κ in the analytic solutions and ξ in the numerical ones. A similar behaviour is observed also for the other PDF combinations.

To conclude this section, we point out that resummation-scale uncertainties for the evolution of α_s and PDFs were treated as distinct in our previous studies [1, 16]. However, the analysis presented above suggests that this is not necessary. Indeed, the variable λ , defined in Eq. (3.4) and entering the analytic evolution of PDFs, arises directly from the evolution of the coupling. As a consequence, we deduce that variations of κ in analytic solutions for PDFs (and by extension of ξ in numerical solutions) are sufficient to estimate the total RGE systematic uncertainties associated with the evolutions of both α_s and PDFs.

5 Transverse-momentum-dependent distributions

In this section, we examine the evolution of TMDs from the standpoint of RGE systematic uncertainties. We give a more detailed presentation than in the cases of α_s and PDFs in the previous two sections. Indeed, unlike α_s and PDFs, TMDs were not treated in our previous work of Ref. [1]. Moreover, new features arise in the case of TMDs, which are associated with the double-logarithmic nature of the evolution. These will help us illustrate further aspects of the resummation scales and the physical meaning of the different scales that enter resummed theoretical predictions.

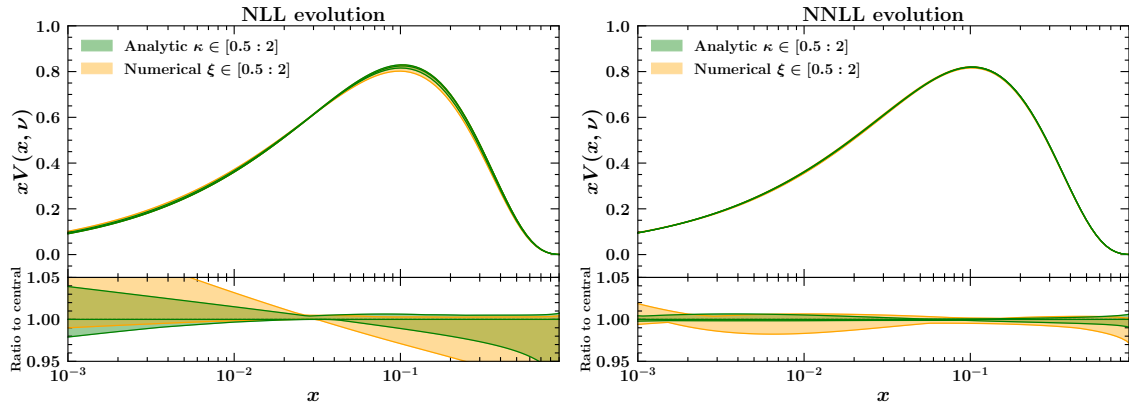


Figure 2. Total-valence PDF xV at $\nu = 100$ GeV evolved analytically and numerically, at NLL (left plot) and NNLL (right plot) accuracy, displayed over the range $x \in [10^{-3} : 1]$. The boundary-condition distributions at $\nu_0 = \sqrt{2}$ GeV and all other theory settings are taken from Ref. [74]. Uncertainty bands correspond to variations of the parameters κ and ξ for analytic and numerical solutions, respectively, in the ranges $\kappa, \xi \in [0.5 : 2]$. Lower panels display the bands normalised to the respective central-value curves obtained with $\kappa = \xi = 1$.

In the following, we start by recalling the TMD evolution equations (Sec. 5.1), then express the solution to these equations through the Sudakov form factor (Sec. 5.2), and present quantitative results for RGE systematics and hysteresis effects (Secs. 5.3 and 5.4). In the light of these results, we comment on the matching of TMDs onto collinear PDFs (Sec. 5.5).

5.1 Evolution

TMD factorisation [36] is commonly carried out in impact-parameter space b , that is, the Fourier-conjugated variable of the partonic transverse momentum k_T . We thus consider the TMD for the partonic species i , $F_i \equiv F_i(x, b, \mu, \zeta)$, which depends on the longitudinal momentum fraction x , the impact parameter b , the renormalisation scale μ , and the rapidity scale ζ . Contrary to collinear distributions, TMDs do not mix upon evolution. Therefore, in order to simplify the notation, we drop the flavour index i . Since in what follows we will mostly be interested in the dependence of F on the scales μ and ζ , we also drop its dependence on x and b .

The TMD F fulfils the following evolution equations,

$$\begin{aligned} \frac{\partial \ln F}{\partial \ln \sqrt{\zeta}} &= \bar{K}(\mu), \\ \frac{\partial \ln F}{\partial \ln \mu} &= \gamma(\mu, \zeta), \end{aligned} \tag{5.1}$$

where γ and \bar{K} are the anomalous dimensions of the evolution in μ and $\sqrt{\zeta}$, respectively.

Appropriate boundary conditions are needed to solve these evolution equations. With the definition

$$\mu_b = \frac{2e^{-\gamma_E}}{b}, \tag{5.2}$$

where γ_E is the Euler-Mascheroni constant, it turns out that convenient boundary-condition scales for the differential equations in Eq. (5.1) are $\mu_0 = \mu_b$ and $\zeta_0 = \mu_b^2$, such that $F(\mu_0, \zeta_0) = F(\mu_b, \mu_b^2)$ is assumed to be known. Without loss of generality, we also set $\zeta = M^2$ as a final rapidity scale,⁶ where M is the hard-scattering scale of the process under consideration. Moreover, we also set $\mu = M$. As we will argue below, variations of the resummation-scale parameter κ introduced in Sec. 2 automatically account for variations of μ around M .

Under these conditions, the differential equations in Eq. (5.1) are solved by

$$F(M, M^2) = \exp \left[\overline{K}(M) \ln \frac{M}{\mu_b} + \int_{\mu_b}^M \frac{d\mu'}{\mu'} \gamma(\mu', \mu_b^2) \right] F(\mu_b, \mu_b^2). \quad (5.3)$$

Besides, the equality of the crossed second derivatives of F yields

$$\frac{\partial \ln F}{\partial \ln \mu \ln \sqrt{\zeta}} = \frac{d\overline{K}}{d \ln \mu} = \frac{d\gamma}{d \ln \sqrt{\zeta}} = -\gamma_K(a_s(\mu)), \quad (5.4)$$

where γ_K is the cusp anomalous dimension. Eq. (5.4) can be solved for \overline{K} and γ using respectively $\mu = \mu_b$ and $\zeta = \mu^2$ as boundary-condition scales, yielding

$$\begin{aligned} \overline{K}(\mu) &= K(a_s(\mu_b)) - \int_{\mu_b}^{\mu} \frac{d\mu'}{\mu'} \gamma_K(a_s(\mu')), \\ \gamma(\mu, \zeta) &= \gamma_F(a_s(\mu)) - \gamma_K(a_s(\mu)) \ln \frac{\sqrt{\zeta}}{\mu}, \end{aligned} \quad (5.5)$$

with $K(a_s(\mu_b)) = \overline{K}(\mu_b)$ and $\gamma_F(a_s(\mu)) = \gamma(\mu, \mu^2)$. The relations in Eq. (5.5) can be plugged into Eq. (5.3), finally giving

$$F(M, M^2) = \exp \left\{ K(a_s(\mu_b)) \ln \frac{M}{\mu_b} + \int_{\mu_b}^M \frac{d\mu'}{\mu'} \left[\gamma_F(a_s(\mu')) - \gamma_K(a_s(\mu')) \ln \frac{M}{\mu'} \right] \right\} F(\mu_b, \mu_b^2). \quad (5.6)$$

All of the anomalous dimensions in Eq. (5.6) admit perturbation expansions as power series in α_s , as follows,

$$\begin{aligned} K(a_s(\mu)) &= \sum_{n=0}^{\infty} a_s^{n+1}(\mu) K^{(n)}, \\ \gamma_F(a_s(\mu)) &= \sum_{n=0}^{\infty} a_s^{n+1}(\mu) \gamma_F^{(n)}, \\ \gamma_K(a_s(\mu)) &= \sum_{n=0}^{\infty} a_s^{n+1}(\mu) \gamma_K^{(n)}. \end{aligned} \quad (5.7)$$

⁶The choice of ζ is actually immaterial. Any physical observable is written as the convolution of two TMDs, which may be computed at different rapidity scales ζ_1 and ζ_2 . However, their convolution only depends on the product $\zeta_1 \zeta_2 = M^4$, which is fixed by kinematic constraints.

5.2 Sudakov form factor

The solution in Eq. (5.6) can be written as

$$F(M, M^2) = \exp \left[\frac{1}{2} S(M, \mu_b) \right] F(\mu_b, \mu_b^2), \quad (5.8)$$

where S is referred to as *Sudakov form factor*,

$$S(M, \mu_b) = 2K(a_s(\mu_b)) \ln \frac{M}{\mu_b} + 2 \int_{\mu_b}^M \frac{d\mu'}{\mu'} \left[\gamma_F(a_s(\mu')) - \gamma_K(a_s(\mu')) \ln \frac{M}{\mu'} \right]. \quad (5.9)$$

Exploiting the identity

$$K(a_s(\mu_b)) \ln \frac{M}{\mu_b} = - \int_{\mu_b}^M \frac{d\mu'}{\mu'} \left[a_s(\mu') \beta(a_s(\mu')) \frac{dK(a_s(\mu'))}{da_s(\mu')} \ln \frac{M}{\mu'} - K(a_s(\mu')) \right], \quad (5.10)$$

the Sudakov form factor in Eq. (5.9) can be written as

$$\begin{aligned} S(M, \mu_b) &= \int_{\mu_b}^M \frac{d\mu'^2}{\mu'^2} \left[\gamma_F(a_s(\mu')) + K(a_s(\mu')) \right. \\ &\quad \left. - \frac{1}{2} \left(\gamma_K(a_s(\mu')) + a_s(\mu') \beta(a_s(\mu')) \frac{dK(a_s(\mu'))}{da_s(\mu')} \right) \ln \frac{M^2}{\mu'^2} \right]. \end{aligned} \quad (5.11)$$

Defining

$$A(a_s(\mu)) = \frac{1}{2} \gamma_K(a_s(\mu)) + \frac{1}{2} a_s(\mu) \beta(a_s(\mu)) \frac{dK(a_s(\mu))}{da_s(\mu)}, \quad (5.12)$$

$$B(a_s(\mu)) = -\gamma_F(a_s(\mu)) - K(a_s(\mu)),$$

Eq. (5.11) takes the form

$$S(M, \mu_b) = - \int_{\mu_b^2}^{M^2} \frac{d\mu'^2}{\mu'^2} \left[A(a_s(\mu')) \ln \frac{M^2}{\mu'^2} + B(a_s(\mu')) \right], \quad (5.13)$$

As a consequence of Eqs. (5.7) and (5.12), the functions A and B admit the perturbative expansions

$$A(a_s(\mu)) = \sum_{n=1}^{\infty} a_s^n(\mu) A^{(n)}, \quad (5.14)$$

$$B(a_s(\mu)) = \sum_{n=1}^{\infty} a_s^n(\mu) B^{(n)},$$

and their perturbative coefficients can be related to those of the anomalous dimensions γ_K , γ_F , and K . Since the logarithmic accuracy $N^k\text{LL}$ is achieved by computing A at $N^k\text{LO}$ and

B at N^{k-1} LO, we have, up to N^3 LL accuracy,

$$\begin{aligned}
\text{LL} : A^{(1)} &= \frac{1}{2}\gamma_K^{(0)}, \\
\text{NLL} : A^{(2)} &= \frac{1}{2}\gamma_K^{(1)} + \frac{1}{2}\beta_0 K^{(0)}, & B^{(1)} &= -\gamma_F^{(0)} - K^{(0)}, \\
\text{NNLL} : A^{(3)} &= \frac{1}{2}\gamma_K^{(2)} + \frac{1}{2}\beta_1 K^{(0)} + \beta_0 K^{(1)}, & B^{(2)} &= -\gamma_F^{(1)} - K^{(1)}, \\
\text{N}^3\text{LL} : A^{(4)} &= \frac{1}{2}\gamma_K^{(3)} + \frac{1}{2}\beta_2 K^{(0)} + \beta_1 K^{(1)} + \frac{3}{2}\beta_0 K^{(2)}, & B^{(3)} &= -\gamma_F^{(2)} - K^{(2)}.
\end{aligned} \tag{5.15}$$

Because $K^{(0)} = 0$ (see App. A.3), at LL and NLL the A and B coefficients are proportional, respectively, to the γ_K and γ_F coefficients. Beyond NLL, this proportionality no longer holds [76] due to the contribution of the rapidity anomalous dimension K .

Similarly to the cases of α_s and PDFs, the Sudakov form factor in Eq. (5.13) (or equivalently in Eq. (5.9)) encoding the evolution of TMDs can be computed analytically or numerically. Once again, analytic solutions are obtained by resorting to perturbative expansions, at the price that the evolution equations in Eq. (5.1) are violated by subleading terms.

5.3 RGE systematics

We now exploit the analytic running of the strong coupling in Sec. 3 to obtain the analytic solution to the RGEs that govern the evolution of TMDs. By making the following change of integration variable,

$$t = a_s(\mu_0)\beta_0 \ln \frac{\kappa\mu'}{\mu_0}, \tag{5.16}$$

where μ_0 is the reference scale at which the coupling α_s is measured, the Sudakov form factor S in Eq. (5.13) can be rewritten as

$$S(M, \mu_b) = -\frac{2}{a_s(\mu_0)\beta_0} \int_{\lambda_M}^{\lambda} dt \left[\frac{2tA(a_s(t))}{a_s(\mu_0)\beta_0} - \overline{B}(a_s(t)) \right], \tag{5.17}$$

where we have set

$$\lambda_M = a_s(\mu_0)\beta_0 \ln \frac{\kappa M}{\mu_0} \quad \text{and} \quad \lambda = a_s(\mu_0)\beta_0 \ln \frac{\kappa\mu_b}{\mu_0}, \tag{5.18}$$

and, with slight abuse of notation, denoted by $a_s(t)$ the coupling evaluated in terms of the $g^{(\beta)}$ -functions (see Eq. (3.3)) with argument t . Moreover, we have defined

$$\overline{B}(a_s) = 2A(a_s) \ln \frac{\kappa M}{\mu_0} + B(a_s) = \sum_{n=1}^{\infty} a_s^n \overline{B}^{(n)}. \tag{5.19}$$

We now assume that $\mu_0 \simeq M$ and $\kappa \simeq 1$, so that $\lambda_M \ll 1$. Splitting the integral in Eq. (5.17) as follows,

$$S(M, \mu_b) = -\frac{2}{a_s(\mu_0)\beta_0} \int_0^\lambda dt \left[\frac{2tA(a_s(t))}{a_s(\mu_0)\beta_0} - \bar{B}(a_s(t)) \right] \\ + \frac{2}{a_s(\mu_0)\beta_0} \int_0^{\lambda_M} dt \left[\frac{2tA(a_s(t))}{a_s(\mu_0)\beta_0} - \bar{B}(a_s(t)) \right], \quad (5.20)$$

we are allowed to compute the second integral perturbatively, expanding the running coupling around $t = 0$. In addition, the exponential of this term (see Eq. (5.8)) can be further expanded and truncated at the appropriate order.

The explicit analytic evaluation of the integrals in Eq. (5.20) finally leads to an expression for the Sudakov form factor of the form

$$\exp(S) = g_0(a_s(\mu_0)) \exp \left[Lg_1(\lambda) + g_2(\lambda, \kappa) + a_s(\mu_0)g_3(\lambda, \kappa) + a_s^2(\mu_0)g_4(\lambda, \kappa) + \dots \right], \quad (5.21)$$

where $L = \ln(\kappa\mu_b/\mu_0)$, and the g -functions are expressed in terms of the perturbative coefficients of the functions A and B . The function g_n , with $n > 0$, in Eq. (5.21) resums the N^{n-1} LL tower of logarithms and can be computed in terms of the functions $g_k^{(\beta)}$, with $k \leq n$, responsible for the analytic evolution of α_s . The function g_0 , on the other hand, admits a perturbative expansion that is to be truncated at $\mathcal{O}(a_s^n)$ to achieve N^{n+1} LL accuracy [41]. All ingredients necessary to obtain a N^3 LL accurate Sudakov form factor are given in App. A.3.

The form of the Sudakov form factor in Eq. (5.21) corresponds to the customary formula obtained in the literature on transverse-momentum resummation: see, *e.g.*, Ref. [68]. A comparison of the g -functions given in App. A.3 with those of Ref. [68] shows that the results agree. In this respect, the calculation which we have performed in this section can be viewed as a derivation of Eq. (5.21) alternative to that given in transverse-momentum resummation, based on a different, but equivalent, methodology which starts from the TMD evolution equations in Eq. (5.1).

Interestingly, the agreement between our results and those of Ref. [68] is achieved by making the identifications $\mu_R = \mu_0$ and $Q = \mu_0/\kappa$, where μ_R and Q are, respectively, the renormalisation and resummation scales in the terminology of Ref. [68]. This observation sheds light on the meaning of the different scales which enter resummed theoretical predictions. As regards the renormalisation scale μ_R of Ref. [68], this is to be identified, in our analysis, with the reference scale μ_0 at which the strong coupling is measured. In other words, $a_s(\mu_0)$ is the measured value of the strong coupling used as an input to its running. To be definite, a common choice is $\alpha_s(M_Z) = 0.118$, so that $\mu_0 = M_Z$ and $4\pi a_s(\mu_0) = 0.118$. In this respect, μ_0 does not have the same meaning as a “standard” renormalisation scale used in fixed-order calculations.

As regards the resummation scale Q , introduced in Ref. [68] directly at the level of Sudakov form factor, our analysis illustrates that this can be traced back to the resummation-scale parameter κ introduced in Eq. (2.4) and used in Eq. (3.4) to parameterise subleading

corrections to the evolution of the strong coupling. Indeed, as illustrated by the analyses of α_s and PDFs in Secs. 3 and 4, the presence of a resummation scale is *not* a prerogative of the resummation of Sudakov (double) logarithms. As a matter of fact, it emerges whenever a resummation takes place as a consequence of the truncation of the anomalous dimensions that govern the relevant RGEs. The resummation scale thus defined originates from the running of the strong coupling, which feeds through the resummation as an expansion parameter of the anomalous dimensions.

We will next move to considering the numerical solution to Eq. (5.13). Analogously to the previous sections, this is achieved by displacing the argument of α_s from μ to $\xi\mu$ in the perturbative expansion of the functions A and B in Eq. (5.14). We refrain from showing the corresponding expansions. The integral in Eq. (5.13) is then computed numerically. As in the cases of α_s and PDFs, variations of ξ in numerical solutions correspond to variations of κ in analytic solutions and can thus be used to estimate RGE systematic uncertainties.

5.4 Hysteresis and perturbative uncertainty on the Sudakov form factor

As an application of the formalism discussed in the previous subsection, we now illustrate a manifestation of the perturbative hysteresis in the analytically computed Sudakov form factor. We then assess the perturbative uncertainty on the Sudakov form factor from variations of the resummation scales. In view of applications to the transverse-momentum spectrum in DY production presented in the next sections, we only consider the case of quark TMDs, leaving gluons aside.

We start by noting that the scale M in the logarithm that multiplies the function A in Eq. (5.13) is to be identified with the rapidity scale ζ . However, as observed above, the value of ζ is fixed by the external kinematics and can be set to the hard scale M throughout. We thus write the Sudakov form factor, controlling the evolution of a TMD from the scale μ_1 to the scale μ_2 at a given hard scale M , as

$$S(\mu_2, \mu_1; M) = - \int_{\mu_1^2}^{\mu_2^2} \frac{d\mu'^2}{\mu'^2} \left[A(a_s(\mu')) \ln \frac{M^2}{\mu'^2} + B(a_s(\mu')) \right]. \quad (5.22)$$

Perturbative hysteresis is characterised by $S(\mu_2, \mu_1; M) + S(\mu_1, \mu_2; M) \neq 0$. Unlike the case of a numerical evaluation, the analytic Sudakov factor computed in terms of the g -functions leads to perturbative hysteresis. To assess its magnitude, we observe that the g -functions are computed by assuming that the upper integration limit in Eq. (5.22), μ_2 , is of the order of the hard scale M , and that this assumption allows any displacement of μ_2 from M to be reabsorbed into the function B (see Eq. (5.19)). In order to compute $S(\mu_2, \mu_1; M) + S(\mu_1, \mu_2; M)$, we release this assumption and rewrite the Sudakov form factor as follows,

$$S(\mu_2, \mu_1; M) = - \int_{\mu_1^2}^{\mu_2^2} \frac{d\mu'^2}{\mu'^2} \left[A(a_s(\mu')) \ln \frac{\mu_2^2}{\mu'^2} + B(a_s(\mu')) \right] - 2 \ln \frac{M}{\mu_2} \int_{\mu_1^2}^{\mu_2^2} \frac{d\mu'^2}{\mu'^2} A(a_s(\mu')). \quad (5.23)$$

The first integral can now be computed analytically and expressed in terms of the usual g -functions,

$$- \int_{\mu_1^2}^{\mu_2^2} \frac{d\mu'^2}{\mu'^2} \left[A(a_s(\mu')) \ln \frac{\mu_2^2}{\mu'^2} + B(a_s(\mu')) \right] = Lg_1(\lambda) + g_2(\lambda) + a_s(\mu_2)g_3(\lambda) + \dots \quad (5.24)$$

with

$$L = \ln \frac{\mu_1}{\mu_2} \quad \text{and} \quad \lambda = a_s(\mu_2)\beta_0 L. \quad (5.25)$$

The integral in the second term of the r.h.s. of Eq. (5.23) can also be computed order by order in perturbation theory using the analytic running of the strong coupling, yielding⁷

$$2 \int_{\mu_1^2}^{\mu_2^2} \frac{d\mu'^2}{\mu'^2} A(a_s(\mu')) = h_1(\lambda) + a_s(\mu_2)h_2(\lambda) + a_s^2(\mu_2)h_3(\lambda) + \dots, \quad (5.26)$$

Up to NLL accuracy, and setting $\kappa = 1$, we find

$$h_1(\lambda) = \frac{4A^{(1)}}{\beta_0} \ln(1-\lambda), \quad (5.27)$$

$$h_2(\lambda) = \frac{4A^{(1)}b_1}{\beta_0} \frac{\lambda + \ln(1-\lambda)}{1-\lambda} - \frac{4A^{(2)}}{\beta_0} \frac{\lambda}{1-\lambda}.$$

This generalisation of the Sudakov form factor enables us to compute the quantity $S(\mu_2, \mu_1; M) + S(\mu_1, \mu_2; M)$. For simplicity, we set $M = \mu_2$ so that the ‘‘forward’’ Sudakov form factor $S(\mu_2, \mu_1; \mu_2)$ can be evaluated using the g -functions only. The ‘‘backward’’ Sudakov form factor $S(\mu_1, \mu_2; \mu_2)$ is instead computed using the generalisation in Eq. (5.23), that is,

$$S(\mu_1, \mu_2; \mu_2) = \tilde{L}g_1(\tilde{\lambda}) + g_2(\tilde{\lambda}) + a_s(\mu_1)g_3(\tilde{\lambda}) + \dots \quad (5.28)$$

$$- \tilde{L} \left[h_1(\tilde{\lambda}) + a_s(\mu_1)h_2(\tilde{\lambda}) + a_s^2(\mu_1)h_3(\tilde{\lambda}) + \dots \right],$$

where

$$\tilde{L} = \ln \frac{\mu_2}{\mu_1} \quad \text{and} \quad \tilde{\lambda} = a_s(\mu_1)\beta_0 \tilde{L}. \quad (5.29)$$

At LL, the Sudakov form factor does not produce any perturbative hysteresis. To see this, we simply need to consider the functions g_1 and h_1 . Using the LL evolution of the strong coupling we find

$$\tilde{\lambda} = -\frac{\lambda}{1-\lambda}, \quad (5.30)$$

so that

$$g_1(\tilde{\lambda}) = \frac{4A^{(1)}}{\beta_0} \frac{\lambda + (1-\lambda)\ln(1-\lambda)}{\lambda} \quad \text{and} \quad h_1(\tilde{\lambda}) = -\frac{4A^{(1)}}{\beta_0} \ln(1-\lambda), \quad (5.31)$$

which immediately implies that $S(\mu_2, \mu_1; \mu_2) + S(\mu_1, \mu_2; \mu_2) = 0$.

Beyond LL, this equality is broken by the analytic solution. To show this, in Fig. 3 we plot the quantity $S(\mu_2, \mu_1; \mu_2) + S(\mu_1, \mu_2; \mu_2)$ both at LL and NLL as a function of μ_1

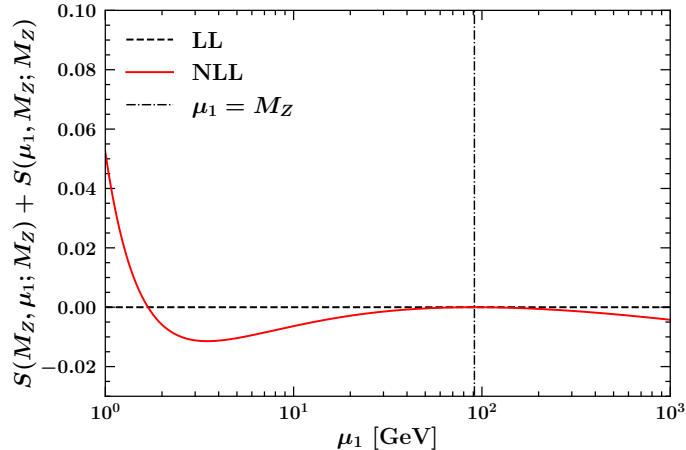


Figure 3. Perturbative hysteresis of the analytic Sudakov form factor at LL and NLL accuracies as a function of the scale μ_1 in the range $\mu_1 \in [1 : 1000]$ GeV. The strong-coupling boundary condition $\alpha_s(M_Z) = 0.118$ is used. The vertical dot-dashed line indicates the scale $\mu_1 = M_Z$ where the boundary condition on α_s is set. At this scale the NLL hysteresis touches zero.

setting $\mu_2 = M_Z$ and $\alpha_s(M_Z) = 0.118$. As expected, the LL curve is identically zero over the entire range in μ_1 considered. At NLL, as a consequence of the perturbative hysteresis, the curve deviates from zero. Deviations are enhanced at small scales where the value of α_s is largest. At $\mu_1 = M_Z$, where no evolution takes place and both $S(M_Z, \mu_1; M_Z)$ and $S(\mu_1, M_Z; M_Z)$ are separately zero, the NLL curve touches zero but it slowly restarts departing from it at larger scales.

We now turn to assessing the perturbative uncertainty on the Sudakov form factor from variations of the resummation-scale parameters in both analytic and numerical solutions. Fig. 4 shows results for S as a function of μ_b , obtained with $\alpha_s(M_Z) = 0.118$ as a boundary condition to the strong coupling, for NLL, NNLL, and N³LL accuracies. The bands correspond to variations of the resummation-scale parameters κ (analytic solution) and ξ (numerical solution) in the range $[0.5 : 2]$. The upper panel of each plot shows the results for S along with their bands, while the lower panel displays their ratio to the central-scale curves obtained with $\kappa = \xi = 1$. We see a significant reduction of the theoretical systematic uncertainties when moving from NLL to N³LL. While at NLL the uncertainties obtained with the numerical solution are significantly smaller than those obtained with the analytic solution, the size of the uncertainty bands at NNLL and N³LL tends to align. At N³LL, in particular, one can see from the lower inset of the bottom plot of Fig. 4 that in the small- μ_b region, where α_s is largest, the bands are as large as 3-4%, while they tend to shrink to a sub-percent level as μ_b increases. We also note that the uncertainty band for the numerical calculation shrinks to zero at $\mu_b = M_Z$, where the boundary condition on the running of α_s is imposed. This does not happen in the analytic case.

⁷Since the logarithm $\ln(M^2/\mu_2^2)$ is potentially large, the perturbative counting of the second term on the r.h.s. of Eq. (5.23) follows that of the function A in the first term.

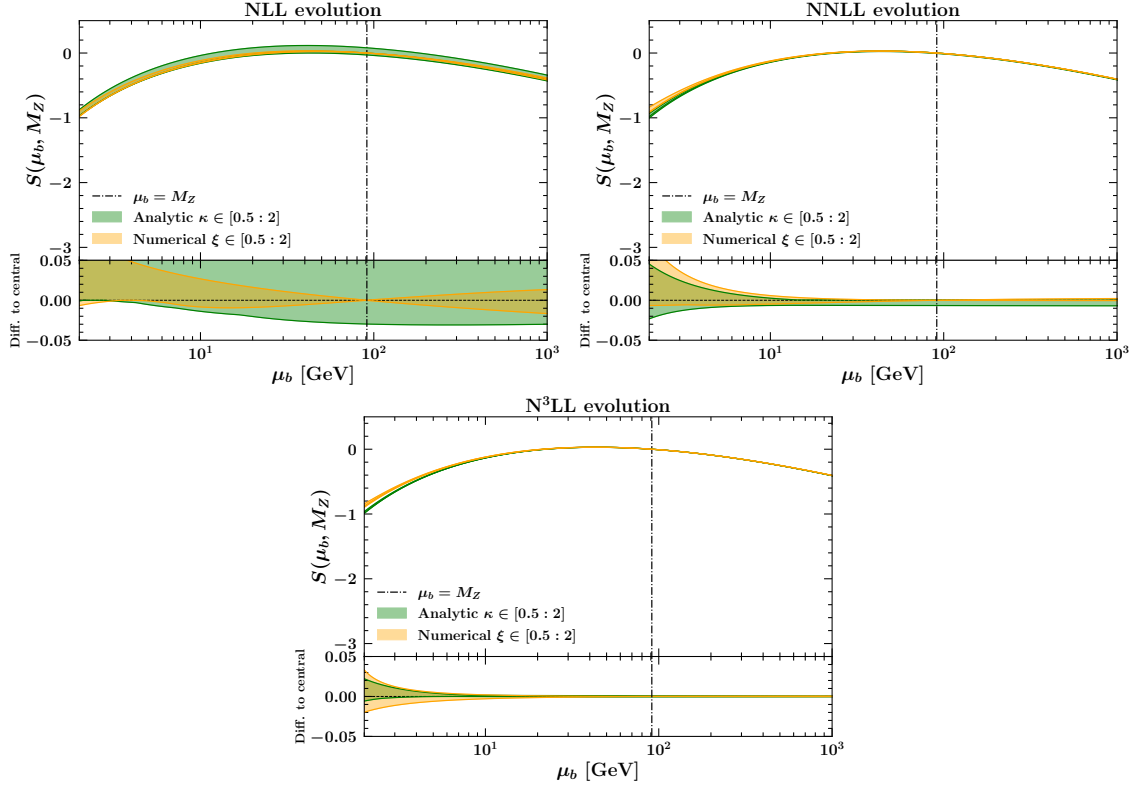


Figure 4. Analytic and numerical Sudakov form factors as functions of μ_b in the range $\mu_b \in [2 : 1000]$ GeV at NLL (top-left plot), NNLL (top-right plot), and N^3 LL (bottom plot) accuracies. The boundary condition of the strong coupling is set at $\alpha_s(M_Z) = 0.118$. Uncertainty bands correspond to variations of the parameters κ and ξ for analytic and numerical solutions, respectively, in the range $\in [0.5 : 2]$. Lower panels display the bands normalised to the respective central-value curves obtained with $\kappa = \xi = 1$.

5.5 Matching on collinear distributions

For small enough values of the impact parameter b , TMDs can be matched onto collinear PDFs via an operator product expansion written in terms of perturbatively computable coefficients. Specifically, the expansion of the TMD distribution F_i can be written as

$$F_i(x, b, \mu, \zeta) = \sum_j \int_x^1 \frac{dy}{y} \bar{C}_{ij}(y, b, \mu, \zeta) f_j\left(\frac{x}{y}, \mu\right) \equiv F(\mu, \zeta), \quad (5.32)$$

where f_j is a collinear PDF, and the functions \bar{C} admit the perturbative expansion

$$\bar{C}_{ij}(y, b, \mu, \zeta) = \sum_{n=0}^{\infty} a_s^n(\mu) \sum_{m=0}^{2n} \sum_{l=0}^m \bar{C}_{ij}^{(n,m,l)}(y) \ln^{m-l}\left(\frac{\mu}{\mu_b}\right) \ln^l\left(\frac{\sqrt{\zeta}}{\mu_b}\right). \quad (5.33)$$

We can now use the matching formula Eq. (5.32) in the r.h.s. of Eq. (5.8) where, due to the scale choice, the logarithmic terms in Eq. (5.33) vanish, giving

$$\bar{C}_{ij}(y, b, \mu_b, \mu_b^2) = \sum_{n=0}^{\infty} a_s^n(\mu_b) \bar{C}_{ij}^{(n,0,0)}(y) \equiv C_{ij}(a_s(\mu_b)), \quad (5.34)$$

that is, a quantity free of any potentially large logarithms and whose scale dependence is entirely driven by the strong coupling. Therefore, dropping the flavour indices and denoting the Mellin convolution with the symbol \otimes , we have

$$F(\mu_b, \mu_b^2) = C(a_s(\mu_b)) \otimes f(\mu_b). \quad (5.35)$$

When computing the Fourier transform with respect to the impact parameter b to obtain physical observables, both the matching coefficient function C and the PDF f are evaluated at the scale μ_b , defined in Eq. (5.2), which can get any positive value. We then resort to the RGEs to write both $C(a_s(\mu_b))$ and $f(\mu_b)$ as resulting from the evolution applied to some fixed reference scale M .

The PDF f obeys the RGE discussed in Sec. 4, whose solution from M to μ_b allows us to formally write⁸

$$f(\mu_b) = \exp \left[- \int_{\mu_b}^M \frac{d\mu'}{\mu'} \gamma(a_s(\mu')) \right] \otimes f(M). \quad (5.36)$$

The coefficient C , depending on the scale μ only through the strong coupling, obeys the following evolution equation⁹

$$\frac{d \ln C(a_s(\mu))}{d \ln \mu} = a_s(\mu) \beta(a_s(\mu)) \frac{d \ln C(a_s(\mu))}{da_s(\mu)}. \quad (5.37)$$

This equation can be used to evolve C from M to μ_b as follows,

$$C(a_s(\mu_b)) = \exp \left[- \int_{\mu_b}^M \frac{d\mu'}{\mu'} a_s(\mu') \beta(a_s(\mu')) \frac{d \ln C(a_s(\mu'))}{da_s(\mu')} \right] \otimes C(a_s(M)). \quad (5.38)$$

Using Eqs. (5.36) and (5.38) in Eq. (5.35), we find

$$F(\mu_b, \mu_b^2) = \exp \left[- \int_{\mu_b}^M \frac{d\mu'}{\mu'} \left(a_s(\mu') \beta(a_s(\mu')) \frac{d \ln C(a_s(\mu'))}{da_s(\mu')} + \gamma(a_s(\mu')) \right) \right] \otimes C(a_s(M)) \otimes f(M). \quad (5.39)$$

Finally, we can plug this expression into Eq. (5.8) and reabsorb the exponential due to the evolution of the PDF f and the coefficient C into the Sudakov form factor. Since these evolutions are single-logarithmic, their effect can be reabsorbed into the function B so that

$$F(M, M^2) = \exp \left[\frac{1}{2} \tilde{S}(M, \mu_b) \right] \otimes C(a_s(M)) \otimes f(M), \quad (5.40)$$

with

$$\tilde{S}(M, \mu_b) = - \int_{\mu_b^2}^{M^2} \frac{d\mu'^2}{\mu'^2} \left[A(a_s(\mu')) \ln \frac{M^2}{\mu'^2} + \tilde{B}(a_s(\mu')) \right], \quad (5.41)$$

where

$$\tilde{B}(a_s(\mu)) = B(a_s(\mu)) + 2a_s(\mu) \beta(a_s(\mu)) \frac{d \ln C(a_s(\mu))}{da_s(\mu)} + 2\gamma(a_s(\mu)). \quad (5.42)$$

⁸As also noted in Sec. 4, this solution implies a number of subtleties related to the flavour structure and the presence of the Mellin convolution.

⁹The logarithm of C is to be interpreted as the logarithm of a matrix in flavour space. In addition, the solution of this evolution equation is subject to the same caveats as the PDF evolution discussed above.

Customarily, the coupling $a_s(M)$ used for the expansion of C is conveniently expressed in terms of the reference value $a_s(\mu_0)$, assuming $\mu_0 \simeq M$ and using the expanded evolution truncated to the relevant order. Analogously, $f(M)$ is usually expressed in terms of $f(\nu_0)$, where ν_0 may be regarded as a scale at which PDFs are fitted, by assuming $\nu_0 \simeq M$ and using the corresponding expanded evolution. Finally, this allows us to write

$$C(a_s(M)) \otimes f(M) = \tilde{C}(a_s(\mu_0)) \otimes f(\nu_0), \quad (5.43)$$

where the perturbative coefficients in the expansion of the function \tilde{C}

$$\tilde{C}(a_s(\mu_0)) = \sum_{n=0}^{\infty} a_s^n(\mu_0) \tilde{C}^{(n)} \quad (5.44)$$

are related, up to N³LL, to those of the function C in Eq. (5.34) as follows,

$$\tilde{C}^{(0)} = \bar{C}^{(0,0,0)},$$

$$\tilde{C}^{(1)} = \bar{C}^{(1,0,0)} + \bar{C}^{(0,0,0)} \otimes \gamma_0 \ln \frac{M}{\mu_0},$$

$$\begin{aligned} \tilde{C}^{(2)} = & \bar{C}^{(2,0,0)} + \bar{C}^{(1,0,0)} \otimes (\gamma_0 + \beta_0) \ln \left(\frac{M}{\nu_0} \right) \\ & + \bar{C}^{(0,0,0)} \otimes \left[\frac{1}{2} \gamma^{(0)} \otimes (\beta_0 + \gamma^{(0)}) \ln^2 \left(\frac{M}{\nu_0} \right) + \gamma^{(1)} \ln \left(\frac{M}{\nu_0} \right) + \beta_0 \gamma^{(0)} \ln \left(\frac{M}{\mu_0} \right) \ln \left(\frac{M}{\nu_0} \right) \right]. \end{aligned} \quad (5.45)$$

Finally, the TMD distribution is evaluated as

$$F(M, M^2) = \exp \left[\frac{1}{2} \tilde{S}(M, \mu_b) \right] \otimes \tilde{C}(a_s(\mu_0)) \otimes f(\nu_0). \quad (5.46)$$

This result, when used to compute physical cross sections, reproduces the usual implementation of transverse-momentum resummation (see, *e.g.*, Refs. [49, 53, 68]). The advantage of this procedure is that it formulates the resummation in a purely analytical fashion, thus limiting as much as possible the amount of possibly expensive numerical computations. It also exposes all the relevant scales (M, μ_0, ν_0, μ_b) allowing for their variations as a proxy to estimate theoretical uncertainties.

On the other hand, this procedure is also affected by limitations which may obscure the meaning of some of the scales. In particular, the scales μ_0 and ν_0 are taken to be of the order of the physical hard scale M . Our analysis illustrates that μ_0 and ν_0 , which are usually denoted by μ_R and μ_F in transverse-momentum-resummation literature, correspond to the reference scales at which strong coupling and PDFs are measured (fitted). We thus observe that the traditional implementation of transverse-momentum resummation implies that both the strong coupling and the PDFs are measured at a scale of the order of the hard scale of the process. To make a specific example, consider DY production with an invariant mass of the lepton pair M around the mass of the Z boson M_Z . In this case,

the formulation discussed above requires $\mu_0 \simeq M_Z$ and a_s is indeed typically measured at this scale with value $\alpha_s(M_Z) = 0.118$. However, it is also necessary that $\nu_0 \simeq M_Z$, but this constraint is usually not fulfilled. As a matter of fact, modern PDF fits are performed assuming $\nu_0 \simeq 1$ GeV, which is far apart from M_Z . A possibility to address this issue would be to extract PDFs by setting ν_0 to a scale of order M_Z . Of course, for hard scales M far away from M_Z the problem would arise again.

Conversely, a numerical formulation of transverse-momentum resummation allows us to relax the constraints $\mu_0 \simeq \nu_0 \simeq M$, while still being able to provide a reliable estimate of perturbative corrections by means of variations of the parameter ξ . Indeed, as we discussed above, our analysis indicates that the scales μ_0 and ν_0 are *not* to be considered as arbitrary scales on the same footing as the usual renormalisation and factorisation scales that appear in fixed-order calculations. Specifically, in our approach, there is little to be gained in varying them because, in principle, this would require re-measuring α_s and PDFs at the new scales. Rather, it is more sensible to keep μ_0 and ν_0 fixed and vary α_s and PDFs within their experimental uncertainties.

6 Physical observables

We devote this section to setting up the stage for our analysis of RGE systematics in physical observables for precision physics at high-energy colliders. We will consider the structure functions in inclusive electron-proton (ep) deep-inelastic-scattering (DIS) through a neutral vector boson with negative virtuality Q (Sec. 6.1), and the transverse-momentum (q_T) spectrum of a lepton pair with invariant mass M in inclusive Drell-Yan (DY) production in proton-proton (pp) collisions (Sec. 6.2). The former observable is characterised by single-logarithmic enhancements, which are tamed by means of the evolution of α_s and PDFs discussed in Secs. 3 and 4.¹⁰ The latter observable features two regimes: $q_T \simeq M$ and $q_T \ll M$. The region $q_T \simeq M$, similarly to DIS, is characterised by single-logarithmic enhancements related to α_s and PDFs that are resummed accordingly. In contrast, the region $q_T \ll M$ is affected by double logarithms that are resummed by means of the Sudakov form factor treated in Sec. 5, controlling the evolution of TMD distributions. In the following, we will discuss how to construct the respective observables and account for all sources of perturbative uncertainties.

In our discussion, we assume that the strong coupling is known at a reference scale μ_0 ($\alpha_s(\mu_0)$) and the PDFs are known at a reference scale ν_0 ($f(\nu_0)$). These reference-scale quantities come with associated uncertainties, which do not have a perturbative origin. They can be incorporated in our calculations, as we will do below, but they do not constitute the focal point of our discussion. Rather, our focus is on perturbative RGE systematic uncertainties, associated with the evolution of α_s and PDFs from the reference scales, μ_0 and ν_0 , to the scales μ and ν relevant to the physical observables. To this purpose, we will use numerical solutions at the appropriate theoretical accuracy with a value of the

¹⁰Additional logarithmic corrections, requiring further resummations beyond those in Secs. 3 and 4, arise in DIS for Bjorken- x_B regions near $x_B \rightarrow 0$ and $x_B \rightarrow 1$. We do not address them here.

resummation-scale parameter ξ of order $\mathcal{O}(1)$.¹¹ Therefore, the evolved α_s and PDFs will also depend parametrically on ξ (*i.e.*, $\alpha_s \equiv \alpha_s(\mu; \xi)$ and $f \equiv f(x, \mu; \xi)$), whose value can be varied to estimate the ensuing uncertainty.

Next, we address the question of defining the perturbative accuracy of a given calculation. In this respect, we will use a fixed-order counting (LO, NLO, NNLO, etc.) to label the relative accuracy in terms of powers of α_s of partonic cross sections and anomalous dimensions. We will instead use the logarithmic counting (LL, NLL, NNLL, etc.) to label the towers of logarithms that are resummed by means of RGEs. When combining fixed-order and resummed calculations to compute a physical observable, the two accuracies are not independent. Indeed, resummation usually comes with a fixed-order (*i.e.*, not logarithmically enhanced) component which also contributes towards the logarithmic counting. Examples are the g_0 functions in the evolution of both PDFs (Eq. (A.5)) and TMDs (Eq. (A.11)), as well as the matching functions in the case of TMDs (Eq. (5.33)). As a consequence, when combined with a fixed-order calculation, the accuracy of resummation is required to be such that it does not deteriorate the fixed-order accuracy. We will substantiate this discussion below when discussing the specific cases of DIS structure functions and DY q_T spectrum.

6.1 Inclusive deep-inelastic electron-proton scattering

One of the simplest examples of observable at high-energy colliders, and yet very important for PDF determinations, is that of the structure functions $\mathcal{F} = F_2, F_L, xF_3$ in (unpolarised) inclusive deep-inelastic ep scattering. These observables obey *collinear factorisation*¹² and therefore they are computed as Mellin convolutions, denoted by the symbol \otimes , over the partonic longitudinal-momentum fraction x between a set of partonic cross sections $\hat{\mathcal{F}}$ and the PDFs f :¹³

$$\mathcal{F}(Q) = \hat{\mathcal{F}} \left(a_s(\mu_R; \xi), \frac{\mu_R}{Q}, \frac{\mu_F}{Q} \right) \otimes f(\mu_F; \xi), \quad (6.1)$$

where Q is the (negative) virtuality of the neutral vector boson (Z/γ^*) that mediates the process. To simplify the notation, we have dropped from Eq. (6.1) all non-scale dependences; these include the Bjorken variable x_B , the partonic longitudinal-momentum fraction x , and the flavour indices. The partonic cross section $\hat{\mathcal{F}}$ at N^pLO accuracy is computed in perturbation theory truncating its expansion at order p in α_s :¹⁴

$$\hat{\mathcal{F}} \left(a_s(\mu_R; \xi), \frac{\mu_R}{Q}, \frac{\mu_F}{Q} \right) = \sum_{n=0}^p a_s^n(\mu_R; \xi) \sum_{i=0}^n \sum_{j=0}^i \hat{\mathcal{F}}^{(n,i,j)} \ln^{i-j} \left(\frac{\mu_R}{Q} \right) \ln^j \left(\frac{\mu_F}{Q} \right). \quad (6.2)$$

¹¹Having established in the previous sections the equivalence between analytic and numerical solutions for all relevant RGEs, in the applications that follow we will employ the numerical solutions throughout.

¹²Appropriate generalisations of the factorisation are needed in DIS for regions near $x_B \rightarrow 0$ and $x_B \rightarrow 1$.

¹³In Eq. (6.1), we are implicitly neglecting the mass m_h of heavy quarks (mostly charm and bottom). Corrections due to the finiteness of m_h can be accounted for and they take the form of powers of m_h/Q in the partonic cross sections. Large logarithms of the same ratio are resummed into the heavy-quark PDFs.

¹⁴When $\mathcal{F} = F_L$, the $\mathcal{O}(\alpha_s^0)$ contribution to $\hat{\mathcal{F}}$ is zero. Therefore, its perturbative expansion effectively starts from $n = 1$ so that, strictly speaking, a truncation of the series in Eq. (6.2) at order p for F_L should be labelled as N^{p-1}LO. However, in DIS measurements F_L is usually combined with F_2 and xF_3 whose perturbative expansions instead do start from $n = 0$. For this reason, we truncate the perturbative series of F_L at the same absolute order p as F_2 and xF_3 and yet label its accuracy as N^pLO.

Strong coupling a_s and PDFs f are evolved using the solution to their respective RGEs. As noted above, the logarithmic accuracy of the evolutions is bound by the fixed-order accuracy of the partonic cross section $\hat{\mathcal{F}}$. Using Eq. (4.1), one has that N^kLL accuracy is achieved by computing $g_0^{(\gamma)}$ at $\mathcal{O}(\alpha_s^k)$. As a consequence, the minimal accuracy of PDF (and α_s) evolution that preserves the N^kLO accuracy of the partonic cross section is N^kLL. Conventionally, computations of \mathcal{F} that combine N^kLO partonic cross sections with N^kLL evolutions are simply labelled as N^kLO.

Finally, we note that the expansion in Eq. (6.2) shows that renormalisation and factorisation scales, μ_R and μ_F , have to be of order $\mathcal{O}(Q)$ to avoid spoiling the convergence of the perturbative series. Alongside, we already argued that the resummation-scale parameter ξ involved in the evolution of α_s and PDFs is to be of order $\mathcal{O}(1)$. Thus, an estimate of the perturbative uncertainties on \mathcal{F} can be achieved by varying μ_R and μ_F around Q , and ξ around 1, by a conventional factor of two. We will present quantitative results for F_2 , F_L , and xF_3 at NNLO accuracy in Sec. 7.1.

6.2 Transverse-momentum spectrum in Drell-Yan production

The inclusive production of a lepton pair with large invariant mass M in pp collisions with centre-of-mass energy \sqrt{s} is referred to as DY production. The transverse-momentum (q_T) spectrum of the lepton pair is a phenomenologically interesting observable, in which q_T introduces an additional scale on top of M that allows one to define two possible regimes: $q_T \simeq M$ and $q_T \ll M$. In the following sections, we will discuss theoretical predictions in both regimes, finally showing how to merge them.

6.2.1 Large- q_T regime

For $q_T \simeq M$, we are in a single-scale regime in which the q_T -differential cross section obeys collinear factorisation, and therefore shares many features with the DIS structure functions discussed in Sec. 6.1. Schematically, it factorises as

$$\frac{d\sigma}{dq_T}(q_T \simeq M, M, s) = \frac{d\hat{\sigma}}{dq_T}\left(\frac{q_T}{M}, \frac{M}{s}, a_s(\mu_R; \xi), \frac{\mu_R}{M}, \frac{\mu_F}{M}\right) \otimes f_1(\mu_F; \xi) \otimes f_2(\mu_F; \xi), \quad (6.3)$$

where we have omitted non-scale variables and flavour indices, and, as usual, used the short-hand symbol \otimes to indicate Mellin convolutions over the partonic longitudinal-momentum fractions. For $q_T \neq 0$, the partonic cross section at N^pLO accuracy reads

$$\begin{aligned} \frac{d\hat{\sigma}}{dq_T}\left(\frac{q_T}{M}, \frac{M}{s}, a_s(\mu_R; \xi), \frac{\mu_R}{M}, \frac{\mu_F}{M}\right) = \\ \sum_{n=0}^p a_s^{n+1}(\mu_R; \xi) \sum_{i=0}^n \sum_{j=0}^i D^{(n,i,j)}\left(\frac{q_T}{M}, \frac{M}{s}\right) \ln^{i-j}\left(\frac{\mu_R}{M}\right) \ln^j\left(\frac{\mu_F}{M}\right). \end{aligned} \quad (6.4)$$

As in the case of DIS, N^kLO accuracy at the level of the observable in Eq. (6.3) is obtained by combining N^kLO partonic cross sections with N^kLL evolution for α_s and PDFs. However, we are also allowed to use N^{k+1}LL evolutions with N^kLO partonic cross sections, which we

will do below. The reason for this stems from the way large- and small- q_T regions are combined, see Sec. 6.2.3. Similarly to the case of DIS structure functions, perturbative uncertainties are estimated by varying μ_R and μ_F around the hard scale M , and ξ around one by a conventional factor of two. Numerical results for the large- q_T spectrum in DY production accurate at LO and NLO will be presented in Sec. 7.2.

6.2.2 Small- q_T regime

For $q_T \ll M$, the q_T -differential DY cross section obeys *TMD factorisation*, *i.e.*, it can be written as a convolution over the partonic transverse momentum k_T of two quark TMDs. This convolution is disentangled under Fourier transformation with respect to k_T , which introduces the conjugate variable b and brings the cross section to the form

$$\frac{d\sigma}{dq_T}(q_T \ll M, M, s) = \sigma_0 H\left(a_s(\mu; \xi), \frac{\mu}{M}\right) \int_0^\infty db \frac{b}{2} J_0(bq_T) F_1(b, \mu, \zeta_1) F_2(b, \mu, \zeta_2). \quad (6.5)$$

As above, in order to simplify the notation, non-scale variables and flavour indices are omitted. In the expression above, σ_0 is the Born cross section and J_0 is the Bessel function of the first kind. The function H is related to the form factor for the transition $Z/\gamma^* \rightarrow q\bar{q}$ and its perturbative expansion reads

$$H\left(a_s(\mu; \xi), \frac{\mu}{M}\right) = 1 + \sum_{n=1}^p a_s^n(\mu; \xi) \sum_{i=0}^{2n} H^{(n,i)} \ln^i\left(\frac{\mu}{M}\right), \quad (6.6)$$

where the truncation power p is determined by the target logarithmic accuracy (see below). As discussed in Sec. 5.1, we can set $\zeta_1 = \zeta_2 = M^2$ without loss of generality. Moreover, based on the correspondence between variations in κ and ξ illustrated in Sec. 5.4, we can set $\mu = M$, as long as ξ is allowed to vary. We thus rewrite the cross section as

$$\frac{d\sigma}{dq_T}(q_T \ll M, M, s) = \sigma_0 H(a_s(M; \xi), 1) \int_0^\infty db \frac{b}{2} J_0(bq_T) F_1(b, M, M^2) F_2(b, M, M^2). \quad (6.7)$$

RGE systematic uncertainties on the cross section (6.7) due to the evolution of α_s , PDFs, and TMDs can be simultaneously estimated through variations of the resummation-scale parameter ξ .

The theoretical accuracy of Eq. (6.7) is determined by the accuracy of TMDs and hard factor H . In turn, the accuracy of TMDs is determined by Sudakov form factor S and the matching functions C , as well as by the evolution of α_s and PDFs. Numerical results for the small- q_T spectrum in DY production at NNLL and N³LL accuracy will be presented in Sec. 7.2. For definiteness, predictions at NNLL (N³LL) are obtained combining Sudakov form factor at NNLL (N³LL), hard factor H and matching functions C at $\mathcal{O}(\alpha_s)$ ($\mathcal{O}(\alpha_s^2)$), PDFs at NLL (NNLL), and α_s at NNLL (N³LL).

6.2.3 Matching small- q_T and large- q_T regions

The formulas in Eqs. (6.3) and (6.7), which are valid, respectively, in the regions $q_T \simeq M$ and $q_T \ll M$, can be consistently combined to produce predictions accurate over a broader

range in q_T . This procedure is referred to as *matching*. Schematically, the *additive* form of matching reads as follows,

$$\frac{d\sigma}{dq_T}(q_T, M, s) = \frac{d\sigma}{dq_T}(q_T \simeq M, M, s) + \frac{d\sigma}{dq_T}(q_T \ll M, M, s) - \frac{d\sigma}{dq_T} \Big|_{\text{d.c.}}(q_T, M, s), \quad (6.8)$$

where the last term in the r.h.s. is the counter-term (labelled by the subscript “d.c.”, which stands for double-counting) needed to subtract the contribution present in both small- and large- q_T terms. Expressions for the counter-term up to $\mathcal{O}(\alpha_s^2)$ can be found, *e.g.*, in Refs. [50, 53, 68]. We stress that also the counter-term is affected by theoretical systematic uncertainties, which can be estimated in a manner analogous to the fixed-order cross section in Eq. (6.3), *i.e.*, by varying μ_R , μ_F , and ξ .

The implementation of Eq. (6.8) may be accompanied by a damping function f suppressing the difference between the small- q_T term and the counter-term when $q_T \simeq M$. The reason for this is that this difference, although subleading in α_s , may have a numerically non-negligible effect. Eq. (6.8) is then modified to

$$\begin{aligned} \frac{d\sigma}{dq_T}(q_T, M, s) &= \frac{d\sigma}{dq_T}(q_T \simeq M, M, s) \\ &+ f(q_T, M) \left[\frac{d\sigma}{dq_T}(q_T \ll M, M, s) - \frac{d\sigma}{dq_T} \Big|_{\text{d.c.}}(q_T, M, s) \right], \end{aligned} \quad (6.9)$$

where f has to be such that

$$f(q_T, M) \xrightarrow{q_T \ll M} 1 \quad \text{and} \quad f(q_T, M) \xrightarrow{q_T \simeq M} 0. \quad (6.10)$$

For the numerical applications presented in Sec. 7.2, we take the functional form for f given in Ref. [77], which reads

$$f(q_T, M) = \begin{cases} 1 & q_T < kM, \\ \exp \left[-\frac{(kM - q_T)^2}{\delta^2 M^2} \right] & q_T > kM, \end{cases} \quad (6.11)$$

with $k = 0.5$ and $\delta = 0.25$. This damping function ensures that, when $q_T \simeq M$, the second line of Eq. (6.9) is exponentially suppressed leaving only the first line, as appropriate. The matching formula (6.9) also implies that a cancellation between large- q_T term and counter-term is to take place at $q_T \ll M$, so as to leave only the small- q_T piece. From a numerical point of view, this is challenging because both the large- q_T term and the counter-term are logarithmically divergent for $q_T \rightarrow 0$. Therefore, it is of crucial importance that their cancellation is numerically very precise in order not to spoil the small- q_T result. We will study this aspect quantitatively in Sec. 7.2.

When matching the small- q_T and large- q_T regimes, the accuracies of the single components in the r.h.s. of Eq. (6.8) (or Eq. (6.9)) are not independent. The large- q_T and double-counting components have to be computed at the same fixed-order accuracy. This imposes

a constraint on the minimal logarithmic accuracy of the small- q_T calculation. Specifically, at N^k LO accuracy for the large- q_T and double-counting components, the small- q_T needs to include fixed-order components, encoded in the hard function H and matching functions C , to order no lower than $\mathcal{O}(\alpha_s^{k+1})$. In a standard counting, this corresponds to a resummation accuracy of N^{k+2} LL. However, one can also use the so-called “primed” convention by which the N^{k+1} LL accurate Sudakov form factor $\exp(S)$ is associated with $\mathcal{O}(\alpha_s^{k+1})$ H and C , and α_s and PDF evolution at N^{k+1} LL. This produces N^{k+1} LL’ predictions at small q_T that, like N^{k+2} LL, can be matched with N^k LO large- q_T predictions. When considering matched predictions in Sec. 7.2, we will consider the following combinations of small- and large- q_T calculations: NNLL+LO, NNLL’+NLO, and N^3 LL+NLO.

7 Numerical applications

In Sec. 6, we have thoroughly described the observables that we will consider and the theoretical setup for their computation, including the definition of the accuracy and the strategy to estimate theoretical uncertainties. In this section, we will present the ensuing numerical results. However, before moving to discussing them, we first specify the settings that are common to all computations.

Throughout this section, we will use $\alpha_s(M_Z) = 0.118$ [78], with $M_Z = 91.1876$ GeV, as an input to the evolution of the strong coupling, and the MSHT20 PDF set [8] at $\nu_0 = 2$ GeV as an input to the evolution of PDFs. In order to focus the discussion on the estimate of theoretical uncertainties, we will always use the NNLO set from the MSHT20 family as an initial-scale set of PDFs, regardless of the accuracy of the calculation.

All evolutions are performed in the variable-flavour-number scheme (VFNS), in which the number of active flavours n_f that enters the perturbative coefficients of the anomalous dimensions changes by one unit when crossing a heavy-quark threshold. In the case of α_s and PDFs, also appropriate matching conditions at threshold are applied. The values of charm and bottom thresholds are taken from the MSHT20 PDF set and are $m_c = 1.4$ GeV and $m_b = 4.75$ GeV. No top-quark threshold is considered, so that the maximum value attainable for n_f is 5.

All numerical calculations presented below use the code APFEL++ [79, 80]. A private implementation of the calculation of Ref. [81] extracted from the DYTURBO code [49] is used for the computation of the large- q_T DY cross section. The LHAPDF interface [82] is used to access the MSHT20 PDF set at $\nu_0 = 2$ GeV.

We next discuss the single observables.

7.1 Deep-inelastic structure functions

In this subsection, we present quantitative results for the DIS neutral-current structure functions F_2 , F_L and xF_3 at NNLO, and estimate the size of theoretical uncertainties by means of variations of the resummation-scale parameter ξ , the factorisation scale μ_F , and the renormalisation scale μ_R .¹⁵ A thorough description of the theory settings can be found

¹⁵In this subsection, as well as in the following one, each band associated with ξ , μ_F , or μ_R variations is obtained by keeping the other two scales fixed at their central values. Moreover, the bands are obtained as

in Sec. 6.1. We also note that a benchmark of the numerical implementation of the DIS structure functions used here against the code HOPPET [83] has been recently presented in Ref. [84]

In Figs. 5, 6, and 7, we show the x -dependence of F_2 , F_L , and xF_3 , respectively, over a wide interval ranging from $x = 10^{-3}$ up to $x = 0.9$, and for two different values of the virtuality Q of the exchanged vector boson. For F_2 and F_L in Figs. 5 and 6, we chose $Q = 10, 100$ GeV, *i.e.*, one scale significantly below M_Z characterised by mostly photon exchange, and one scale above M_Z where the Z contribution is dominant. For xF_3 in Fig. 7, instead, we chose the scales $Q = 100, 500$ GeV because, at scales below M_Z , this structure function is suppressed by the Z propagator. In these figures, the upper panel of each plot shows the value of the structure function along with its theoretical uncertainty bands, while the lower panel shows its ratio to the central-scale curve obtained with $\mu_R = \mu_F = Q$ and $\xi = 1$.

We observe that the ξ bands are sizeable across the board and are generally comparable to μ_R and μ_F bands, confirming that RGE-related uncertainties are non-negligible and should therefore be taken into account. As a consequence of the fact that the $\mathcal{O}(\alpha_s^0)$ contribution to F_L is identically zero, ξ variations for this structure function are relatively smaller than μ_R and μ_F variations. The picture is different for F_2 and xF_3 , which instead have a non-vanishing $\mathcal{O}(\alpha_s^0)$ contribution and where the ξ bands are generally larger than those associated with μ_R and μ_F . We also observe that ξ variations remain approximately of the same relative size for both values of Q considered, while μ_R and μ_F variations tend to shrink as the scale Q increases. This is an expected behaviour. Indeed, for an N^k LO calculation, the size of μ_R and μ_F variations is roughly proportional to $\alpha_s^{k+1}(Q) \ln^{k+1}(\mu_{R,F}/Q)$. Therefore, their size decreases proportionally to a power of $\alpha_s(Q)$, becoming smaller and smaller as Q grows. Variations of the parameter ξ have a completely different behaviour that we discussed in Sec. 4 (see Eq. (4.4)). The main point here is that these variations generate terms proportional to $(\alpha_s^{k+1}(\xi Q) - \alpha_s^{k+1}(\xi \nu_0)) \ln^{k+1} \xi$, with $\nu_0 = 2$ GeV. The consequence is that, for $Q \gg \nu_0$ and $\xi \sim 1$, the uncertainty is dominated by $\alpha_s^{k+1}(\xi \nu_0)$ no matter how large Q is.

In order to study the Q behaviour of theoretical uncertainties more in detail, in Fig. 8 we show $\Delta F_2/F_2$ as a function of Q in a range between $Q = 2$ GeV and $Q = 500$ GeV at $x = 10^{-2}$, where F_2 is the structure function computed with central scales and ΔF_2 is the deviation caused by each variation. As expected, uncertainties generated by variations of μ_R and μ_F are largest at small scales and decrease as Q increases. On the contrary, the uncertainty related to ξ variations is small at low values of Q , *i.e.*, close to the PDF initial scale, and tends to grow at large Q , remaining roughly of the same relative size for $Q \gtrsim 10$ GeV. A similar behaviour is observed for other kinematic configurations and structure functions.

envelopes of a scan between the quoted bounds, and *not* as a differences between predictions with central scales and the bounds of the variation ranges. This prevents possible non-monotonicities of scale variations from underestimating the corresponding uncertainties.

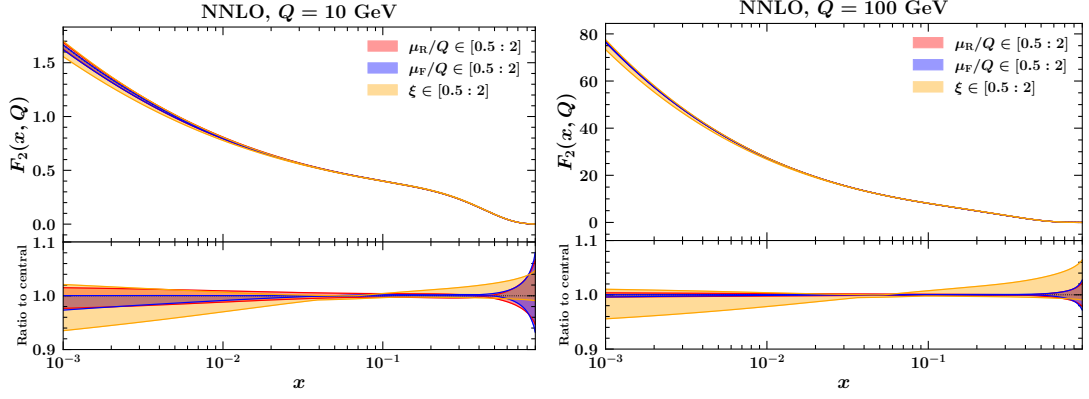


Figure 5. The DIS F_2 structure function at NNLO plotted versus x for two different values of Q . Uncertainty bands associated with variations of renormalisation and factorisation scales, μ_R and μ_F , and resummation-scale parameter, ξ , are also displayed. The lower insets show the predictions normalised to the central-scale curves.

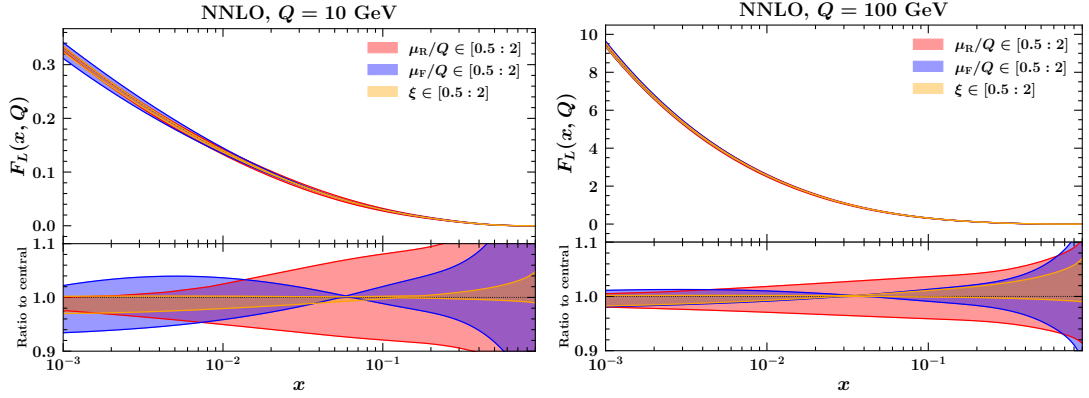


Figure 6. Same as Fig. 5 for F_L .

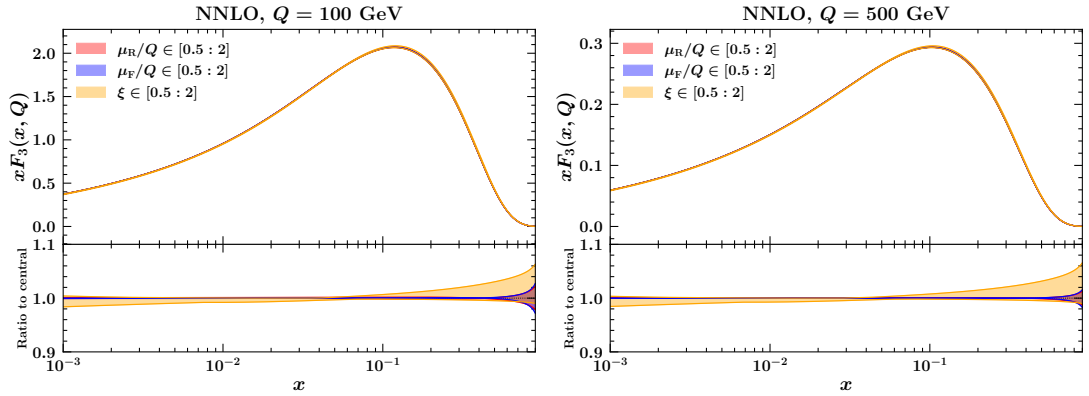


Figure 7. Same as Fig. 5 for $x F_3$.

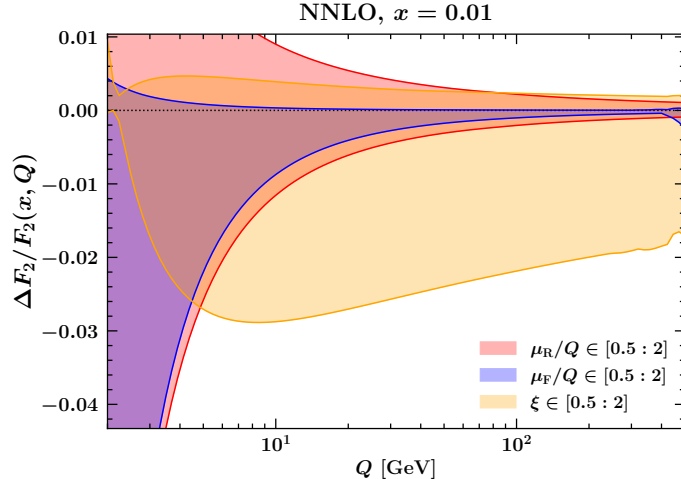


Figure 8. Q -dependence of the ratio $\Delta F_2/F_2$ at NNLO at $x = 10^{-2}$ associated with variations of renormalisation and factorisation scales, μ_R and μ_F , and resummation-scale parameter, ξ .

7.2 Drell-Yan transverse momentum distribution

We now turn to the numerical implementation of our framework in the case of the DY q_T spectrum. We will first address the large- q_T region, then consider the small- q_T region, and finally present results for the matched calculation. As above, we will put particular emphasis on the estimate of theoretical uncertainties.

Fig. 9 shows predictions for the q_T spectrum of a lepton pair with invariant mass $M = M_Z$ and central rapidity, $y = 0$, in DY production in pp collisions at $\sqrt{s} = 13$ TeV in a region ranging between $q_T = 10$ GeV and $q_T = 1000$ GeV. Predictions are computed at LO (left panel) and NLO (right panel) and include uncertainty bands relative to variations of renormalisation scale μ_R , factorisation scale μ_F , and resummation-scale parameter ξ . The upper insets display the cross sections, while the lower insets show their ratios to central-scale predictions. The expected reduction of all of the band widths when moving from LO to NLO is observed. Analogously to DIS structure functions, we also note that the ξ band is generally of the same size of, or even larger than, the μ_R and μ_F bands. This provides a further example of the fact that RGE-related uncertainties can be sizeable and thus need to be taken into proper account.

We now move to the small- q_T region. We consider again the q_T distribution of a lepton pair with invariant mass $M = M_Z$ and rapidity $y = 0$ in DY production in pp collisions at $\sqrt{s} = 13$ TeV. As argued above, this regime is characterised by the resummation of large logarithms of q_T/M . Therefore, its theoretical uncertainty can be estimated by variations of the resummation-scale parameter ξ , which accounts at once for the uncertainty on the evolution of α_s , PDFs, and TMDs. Fig. 10 shows this cross section in the range $q_T \in [0 : 30]$ GeV at NNLL (left panel) and N³LL (right panel) along with its ξ uncertainty. As above, upper insets display the cross sections, while the lower insets show their ratios to central-scale predictions. We observe that, moving from NNLL to N³LL, the uncertainty shrinks

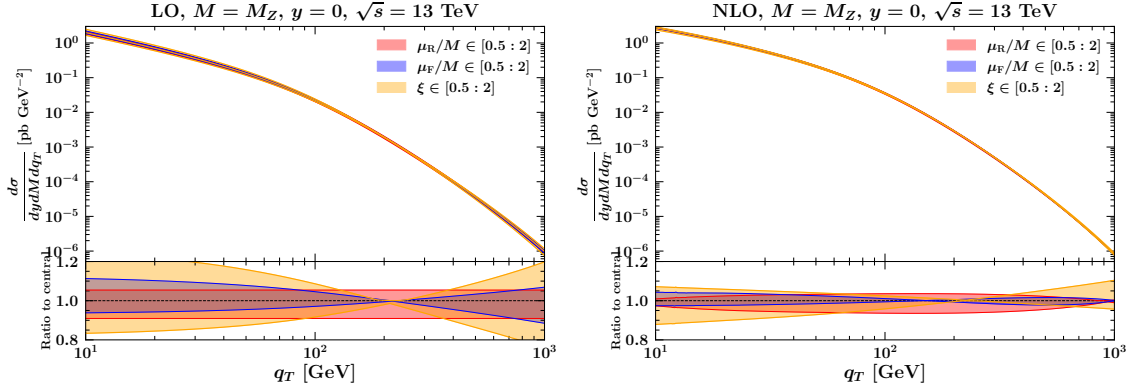


Figure 9. DY large- q_T spectrum of a lepton pair with invariant mass M equal to M_Z and central rapidity ($y = 0$) at LO (left) and NLO (right) accuracies at the 13 TeV LHC. The curves include uncertainty bands associated with variations of resummation scale-parameter ξ , renormalisation scale μ_R , and factorisation scale μ_F . The upper insets display the cross sections, while the lower insets show their ratios to central-scale predictions.

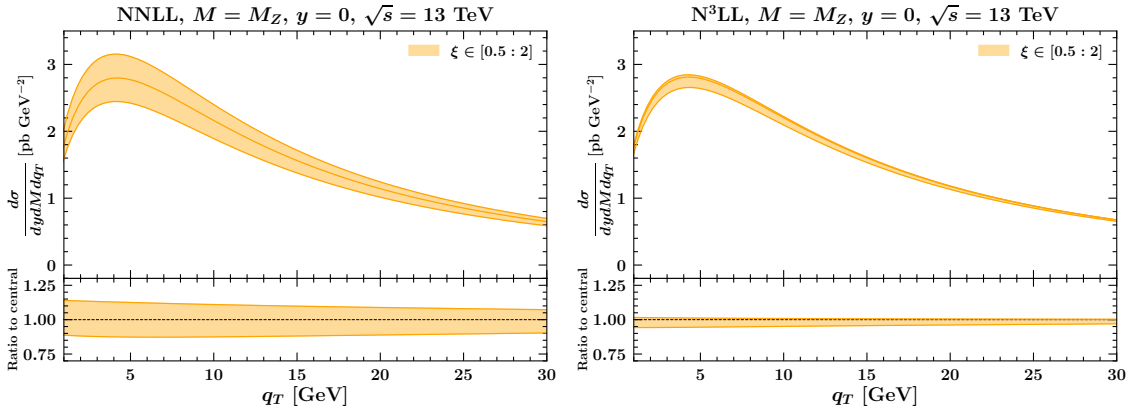


Figure 10. DY small- q_T spectrum of a lepton pair with invariant mass M equal to M_Z and at central rapidity ($y = 0$) at NNLL (left) and N^3 LL (right) accuracies at the 13 TeV LHC. The curves include an uncertainty band associated with variations of resummation scale-parameter ξ . The upper insets display the cross sections, while the lower insets show their ratios to central-scale predictions.

significantly, as expected. Moreover, at both orders, bands are only mildly dependent on q_T , remaining approximately of the same relative size across the whole range considered.

We now address the question of matching small- and large- q_T regimes. In Sec. 6.2.3, we discussed the technical details of this procedure. Before presenting results for the matched cross sections, we study the numerical cancellation between large- q_T and double-counting contributions at $q_T \ll M$. Indeed, a precise cancellation of these terms at small q_T is a requirement in order for the additive matching formula in Eq. (6.9) to work accurately. The cancellation needs to be accurate for all possible choices of the scales. To this purpose,

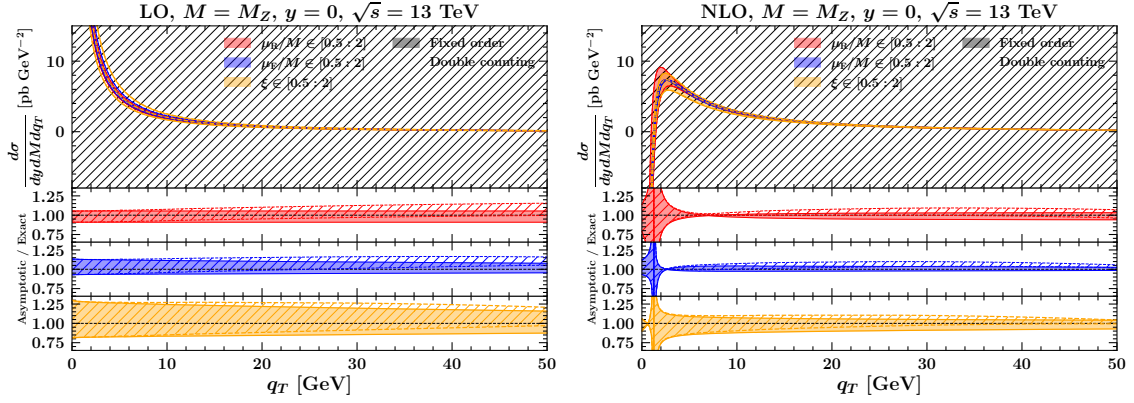


Figure 11. Large- q_T (fixed order) vs. double-coupling terms of Eq. (6.9) in the small- q_T region for the DY spectrum with invariant mass $M = M_Z$ and rapidity $y = 0$ at LO (left) and NLO (right) accuracies at the 13 TeV LHC. The curves include uncertainty bands associated with variations of resummation scale-parameter ξ , renormalisation scale μ_R , and factorisation scale μ_F . The upper insets display the cross sections, while the lower insets show their ratios to central-scale predictions.

in Fig. 11 we show the behaviour of both large- q_T and double-counting cross sections in the small- q_T region at LO (left plot) and NLO (right plot). As above, the kinematics is $M = M_Z$, $y = 0$, and $\sqrt{s} = 13$ TeV. Each curve comes with three different bands associated with renormalisation-scale (red), factorisation-scale (blue), and resummation-scale-parameter (orange) variations. Plain (hatched) bands correspond to the large- q_T (double-counting) calculations. The upper panel of each plot shows the cross sections, while the underlying panels display ratios of each scale variation to the respective central-scale curve. We first note that both LO and NLO calculations are divergent as $q_T \rightarrow 0$, but while the LO is positively divergent, the NLO tends to negative infinity. In spite of this steep behaviour, as seen from the ratio panels, large- q_T and double-counting calculations converge nicely in this region at the level of both central values and single scale variations. This guarantees an accurate implementation of the matching formula, Eq. (6.9), in the $q_T \ll M$ region.

Finally, in Fig. 12 we show matched predictions for the q_T distribution with the same kinematics as above at NNLL + LO (top left), NNLL' + NLO (top right), and N³LL + NLO (bottom) accuracy. The logarithmic accuracy corresponds to the small- q_T calculation while the fixed-order one to the large- q_T calculation, with the counter-term chosen accordingly. The matching allows us to consider at once predictions that range between $q_T = 0$ GeV and $q_T = 100$ GeV. As usual, the upper panels show the cross sections along with scale-variation curves, while the lower panels show their ratios to central-scale predictions. The uncertainty reduction in moving to higher perturbative accuracies is manifest. In particular, while at NNLL + LO uncertainties are roughly at the 10% level all across the range in q_T considered, they reduce to about 5% at N³LL + NLO. We also observe a clear predominance of ξ uncertainties at small and intermediate values of q_T region (up to $q_T \sim 60$ GeV), with renormalisation- and factorisation-scale uncertainties taking over at larger q_T . This

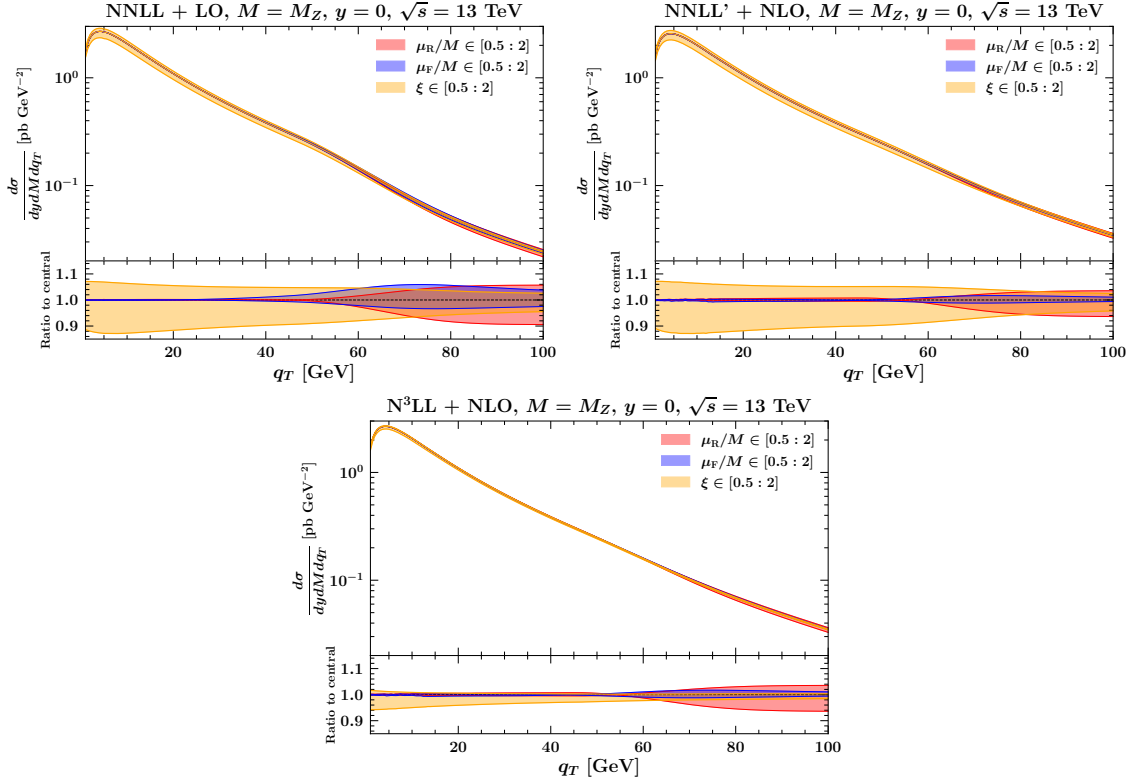


Figure 12. Matched result for the DY q_T spectrum of a lepton pair with invariant mass M equal to M_Z and at central rapidity ($y = 0$) at NLL + LO (top left), NNLL + NLO (top right), and N^3 LL + NLO (right) accuracies at the 13 TeV LHC. The curves include an uncertainty band associated with variations of resummation scale-parameter ξ . The upper insets display the cross sections, while the lower insets show the ratio to central-scale predictions.

behaviour reflects the regions of importance of resummed and fixed-order calculations.

As a last study, in Fig. 13 we consider the N^3 LL + NLO spectrum and, on top of the theoretical-uncertainty band (gray) obtained as an envelope of all scale-variations bands (μ_R, μ_F, ξ), we also show:

- in cyan the band associated to variations of the strong-coupling boundary condition within its uncertainty, $\alpha_s(M_Z) = 0.1180 \pm 0.0009$ [78],
- in magenta the band produced by the error members of the MSHT2020 PDF set [8] at $\nu_0 = 2$ GeV.

The main observation is that all bands are roughly of the same size, but with the theory uncertainty being generally larger. This plot shows that an accurate estimate of theoretical uncertainties, including those of RGE origin, is of crucial importance to achieve a reliable comparison with the accurate data delivered by the LHC.

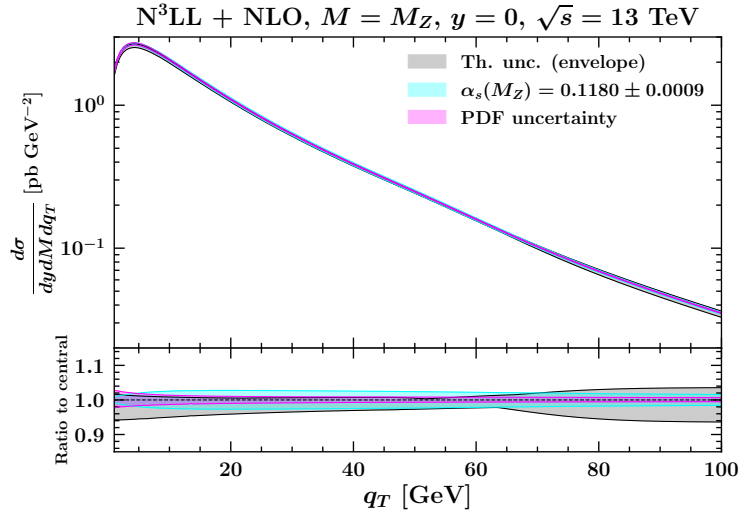


Figure 13. Same as the bottom plot of Fig. 12, *i.e.*, the $N^3\text{LL} + \text{NLO}$ q_T spectrum, where the global theoretical uncertainty (gray), obtained as the envelope of the variations of μ_R , μ_F , and ξ , is compared with the uncertainties associated with the boundary conditions of strong coupling (cyan) and PDFs (magenta).

8 Conclusions

In this work, we have investigated the role of theoretical RGE uncertainties in QCD in the context of high-energy collider phenomenology. We have developed a theoretical framework, inspired by soft-gluon and transverse-momentum resummations, able to take this RGE systematics into account.

The discussion moves from the observation that *analytic* solutions to RGEs may violate their respective evolution equations by terms which are subleading with respect to the perturbative accuracy of the anomalous dimension. A manifestation of these violations is the so-called perturbative hysteresis. However, one of the advantages of analytic solutions is that they expose the potentially large logarithms which are resummed, thus allowing resummation scales to be explicitly introduced (see, *e.g.*, Eq. (2.4)). These scales have the purpose of parameterising subleading corrections to analytic solutions and enable us to estimate the corresponding theoretical uncertainty. An alternative approach to solving RGEs is the *numerical* one. While in this case it is impossible to introduce resummation scales at the level of the solutions, we have shown that this can still be done at the level of anomalous dimensions. To this end, we displace the argument of the coupling α_s in their perturbative expansions so as to generate different anomalous dimensions that differ by subleading terms (see, *e.g.*, Eq. (2.8)). Varying the amount of displacement allows us to compute numerical solutions that are perturbatively equivalent but numerically different. The difference provides an estimate of the associated theoretical uncertainty. Importantly, we have argued that the two seemingly different ways of estimating RGE-related uncertainties in analytic and numerical solutions are in fact in one-to-one correspondence.

In this work, we have treated the single-logarithmic cases of α_s and PDFs, already addressed in Ref. [1], and extended the discussion to the double-logarithmic case of TMDs. In all three cases, we have computed and compared analytic and numerical solutions to the respective RGEs, focusing on the estimate of uncertainties deriving from variations of the resummation scales. In this respect, we have shown quantitatively the general agreement between the two approaches up to high perturbative accuracies.

We then moved on to assessing the impact of RGE-related uncertainties on the perturbative computation of physical observables at high-energy colliders. In this context, we put particular emphasis on comparing resummation-scale uncertainties to renormalisation- and factorisation-scale uncertainties. We considered the cases of structure functions in DIS and of the q_T spectrum in DY production in pp collisions. The former observable is relevant to extractions of PDFs from data, and so is the latter when q_T is large enough. DY at small values of q_T is instead relevant to extractions of TMDs from data, as well as to the precision determination of the electroweak parameters of the Standard Model.

The computation of DIS structure functions obeys collinear factorisation and is characterised by single-logarithmic resummations, encoded in the running of α_s and PDFs. We considered the neutral-current unpolarised structure functions F_2 , F_L , and xF_3 at NNLO accuracy. We observed that resummation-scale uncertainties are generally sizeable and of the same order as (when not larger than) renormalisation- and factorisation-scale variations. A similar picture emerges when studying DY production at large values of q_T at LO and NLO accuracy. Indeed, also this observable undergoes collinear factorisation and is thus affected by single logarithms only.

DY production at small values of q_T obeys TMD factorisation and is characterised by the resummation of double logarithms. Also in this case, we have carried out a detailed study of the impact of resummation-scale uncertainties up to N³LL accuracy. We have examined the potential advantages of the numerical approach over the analytic one, often employed in q_T -resummation literature. In particular, we have discussed the meaning of the different scales entering resummed predictions in the two cases. In our calculation, based on numerical solutions, we employ appropriate reference scales for each of the evolving quantities, and evaluate RGE-related uncertainties only by means of resummation-scale variations.

In order to show that our framework can be consistently applied to single- and double-logarithmic resummations at once, we have also given a quantitative assessment of theoretical uncertainties when large- q_T and small- q_T DY calculations are matched. Here we have compared resummation-scale and renormalisation/factorisation-scale uncertainties (with the latter only stemming from the large- q_T calculation) over a wide range in q_T relevant to DY production at the LHC at 13 TeV. This allowed us to provide a comprehensive estimate of theoretical uncertainties that affect this observable and to compare them to the experimental uncertainties associated with the measured values of α_s and PDFs.

Our results indicate that RGE effects are sizeable and can influence ongoing collider phenomenology programmes. In particular, they are relevant for the assessment of theoretical uncertainties in the extraction of PDFs from data, and for precision physics in DY production at the LHC. In the longer term, they can affect the planning of experiments at

the next energy frontier, for which RGEs are an essential component to relate lower-energy results to physics studies in the kinematic region accessible at future machines.

Acknowledgments

The authors would like to thank S. Camarda, T. Cridge, F. Giuli, S. Glazov, P. Monni, and A. Vicini for stimulating discussions. G.B. would like to express his deepest gratitude to the late Stefano Catani: a caring mentor and colleague, an outstanding scientist and, above all, a wonderful person. V.B. was supported by the European Union’s Horizon 2020 research and innovation programme under grant agreement STRONG 2020 - No 824093.

A Collection of formulas

In this appendix, we collect the g -functions relevant to the implementation of the analytic evolution of α_s (App. A.1), PDFs (App. A.2), and TMDs (App. A.3). Expressions are given in terms of known perturbative coefficients, such as those of the β -function, of the DGLAP splitting functions (in Mellin space), and the A - and B -functions. A numerical implementation of these functions can be found in the codes APFEL++ [79, 80] and MELA [75].

A.1 g -functions for the strong coupling

With reference to Eq. (3.3), the $g^{(\beta)}$ -functions necessary to achieve N³LL accurate evolution of the strong coupling α_s are the following:

$$\begin{aligned}
g_1^{(\beta)}(\lambda) &= \frac{1}{1-\lambda}, \\
g_2^{(\beta)}(\lambda, \kappa) &= -\frac{b_1 \ln(1-\lambda) + \beta_0 \ln \kappa}{(1-\lambda)^2}, \\
g_3^{(\beta)}(\lambda, \kappa) &= \left[b_2 \lambda - b_1^2 \left(\lambda + \ln(1-\lambda) - \ln^2(1-\lambda) \right) \right. \\
&\quad \left. + \beta_0 b_1 (2 \ln(1-\lambda) - 1) \ln \kappa + (\beta_0)^2 \ln^2 \kappa \right] / (1-\lambda)^3, \\
g_4^{(\beta)}(\lambda, \kappa) &= \left[(b_3 - b_2 b_1) \lambda - \frac{1}{2} (b_1^3 - 2 b_2 b_1 + b_3) \lambda^2 + (2 b_1 (b_1^2 - b_2) \lambda - b_2 b_1) \ln(1-\lambda) \right. \\
&\quad \left. + b_1^3 \left(\frac{5}{2} - \ln(1-\lambda) \right) \ln^2(1-\lambda) + (2(b_1^2 - b_2) \lambda \right. \\
&\quad \left. + b_1^2 (5 - 3 \ln(1-\lambda)) \ln(1-\lambda) - b_2) \beta_0 \ln \kappa \right. \\
&\quad \left. + b_1 (-3 \ln(1-\lambda) + \frac{5}{2}) \beta_0^2 \ln^2 \kappa - \beta_0^3 \ln^3 \kappa \right] / (1-\lambda)^4,
\end{aligned} \tag{A.1}$$

with $b_i = \beta_i/\beta_0$. Given our definition of RGE for α_s in Eq. (3.2), the relevant coefficients β_i read [85]

$$\begin{aligned}
\beta_0 &= -2 \left[\frac{11}{3} C_A - \frac{4}{3} T_R n_f \right], \\
\beta_1 &= -2 \left[\frac{34}{3} C_A^2 - \frac{20}{3} C_A T_R n_f - 4 C_F T_R n_f \right], \\
\beta_2 &= -2 \left[\frac{2857}{54} C_A^3 - \frac{1415}{27} C_A T_R n_f - \frac{205}{9} C_F C_A T_R n_f + 2 C_F^2 T_R n_f \right. \\
&\quad \left. + \frac{44}{9} C_F T_R^2 n_f^2 + \frac{158}{27} C_A T_R^2 n_f^2 \right], \\
\beta_3 &= -2 \left[C_A^4 \left(\frac{150653}{486} - \frac{44}{9} \zeta_3 \right) + d_A^{abcd} d_A^{abcd} \left(-\frac{80}{9} + \frac{704}{3} \zeta_3 \right) \right. \\
&\quad + C_A^3 T_R n_f \left(-\frac{39143}{81} + \frac{136}{3} \zeta_3 \right) + C_A^2 C_F T_R n_f \left(\frac{7073}{243} - \frac{656}{9} \zeta_3 \right) \\
&\quad + C_A C_F^2 T_R n_f \left(-\frac{4204}{27} + \frac{352}{9} \zeta_3 \right) + d_F^{abcd} d_A^{abcd} n_f \left(\frac{512}{9} - \frac{1664}{3} \zeta_3 \right) \\
&\quad + 46 C_F^3 T_R n_f + C_A^2 T_R^2 n_f^2 \left(\frac{7930}{81} + \frac{224}{9} \zeta_3 \right) + C_F^2 T_R^2 n_f^2 \left(\frac{1352}{27} - \frac{704}{9} \zeta_3 \right) \\
&\quad + C_A C_F T_R^2 n_f^2 \left(\frac{17152}{243} + \frac{448}{9} \zeta_3 \right) + d_F^{abcd} d_F^{abcd} n_f^2 \left(-\frac{704}{9} + \frac{512}{3} \zeta_3 \right) \\
&\quad \left. + \frac{424}{243} C_A T_R^3 n_f^3 + \frac{1232}{243} C_F T_R^3 n_f^3 \right], \tag{A.2}
\end{aligned}$$

where n_f stands for the number of active quark flavours and $\zeta_i \equiv \zeta(i)$ are the values of Riemann's ζ -function. The colour factors are given by

$$\begin{aligned}
T_R &= \frac{1}{2}, \quad C_A = N_c, \quad C_F = \frac{N_c^2 - 1}{2N_c}, \quad d_A^{abcd} d_A^{abcd} = \frac{N_c^2(N_c^2 + 36)}{24}, \\
d_F^{abcd} d_A^{abcd} &= \frac{N_c(N_c^2 + 6)}{48}, \quad d_F^{abcd} d_F^{abcd} = \frac{N_c^4 - 6N_c^2 + 18}{96 N_c^2}, \tag{A.3}
\end{aligned}$$

with $N_c = 3$.

A.2 g -functions for PDFs

The analytic solution for the evolution of PDFs is given by Eq. (4.1). As discussed in Sec. 4, that formulation strictly applies to Mellin moments of a non-singlet PDF combination. However, the singlet case can be accommodated by promoting the $g^{(\gamma)}$ -functions to 2×2 matrices that couple the evolution of total-singlet and gluon PDFs. In turn, this implies computing exponentials of 2×2 matrices, which can be done in closed form [86]. The x -space solution is then obtained by inverse Mellin transform of the evolved PDF moments. This technology is implemented in the code MELA [75]. An analytic computation directly in x -space is harder to obtain due to the integro-differential nature of the PDF evolution equations in this space. A discretised path-ordered solution could achieve this goal but, to the best of our knowledge, this approach has never been pursued so far.

The functions $g_i^{(\gamma)}$ with $i > 0$ entering the exponential in in Eq. (4.1) and necessary to

achieve NNLL accuracy are the following:

$$\begin{aligned}
g_1^{(\gamma)}(\lambda) &= \frac{\gamma^{(0)}}{\beta_0} \ln \left(g_1^{(\beta)}(\lambda) \right) = -\frac{\gamma^{(0)}}{\beta_0} \ln(1-\lambda), \\
g_2^{(\gamma)}(\lambda, \kappa) &= \frac{\gamma^{(0)}}{\beta_0} \frac{g_2^{(\beta)}(\lambda, \kappa)}{g_1^{(\beta)}(\lambda)} = -\frac{\gamma^{(0)}}{\beta_0} \frac{b_1 \ln(1-\lambda) + \beta_0 \ln \kappa}{1-\lambda}, \\
g_3^{(\gamma)}(\lambda, \kappa) &= \frac{\gamma^{(0)}}{\beta_0} \left[\frac{g_3^{(\beta)}(\lambda, \kappa)}{g_1^{(\beta)}(\lambda)} - \frac{1}{2} \left(\frac{g_2^{(\beta)}(\lambda, \kappa)}{g_1^{(\beta)}(\lambda)} \right)^2 \right] \\
&= \frac{\gamma^{(0)}}{\beta_0} \left[b_2 \lambda - b_1^2 \left(\lambda + \ln(1-\lambda) - \frac{1}{2} \ln^2(1-\lambda) \right) \right. \\
&\quad \left. + \beta_0 b_1 (\ln(1-\lambda) - 1) \ln \kappa + \frac{1}{2} \beta_0^2 \ln^2 \kappa \right] / (1-\lambda)^2. \tag{A.4}
\end{aligned}$$

The first equality in each of the equations above shows how the $g^{(\gamma)}$ -functions are related to the $g^{(\beta)}$ -functions presented in App. A.1.

The function $g_0^{(\gamma)}$ truncated at $\mathcal{O}(\alpha_s^2)$, necessary to achieve NNLL accuracy, reads

$$\begin{aligned}
g_0^{(\gamma),\text{NNLL}}(\lambda, \kappa) &= 1 + \frac{a_s(\mu_0)\lambda}{\beta_0(1-\lambda)} \left(\gamma^{(1)} - b_1 \gamma^{(0)} \right) \tag{A.5} \\
&+ \frac{a_s^2(\mu_0)}{2\beta_0^2(1-\lambda)^2} \left[b_1 \left(\gamma^{(1)} \left(\beta_0 ((\lambda-2)\lambda - 2\ln(1-\lambda)) - 2\lambda^2 \gamma^{(0)} \right) + 2\beta_0^2 \ln \kappa \gamma^{(0)} \right) \right. \\
&+ b_1^2 \gamma^{(0)} \left(\lambda^2 \gamma^{(0)} - \beta_0 ((\lambda-2)\lambda - 2\ln(1-\lambda)) \right) + b_2 \beta_0 (\lambda-2) \lambda \gamma^{(0)} \\
&\left. + \gamma^{(1)} \left(\lambda^2 \gamma^{(1)} - 2\beta_0^2 \ln \kappa \right) - \beta_0 (\lambda-2) \lambda \gamma^{(2)} \right].
\end{aligned}$$

The numerical values of the coefficients β_0 and b_i can be found in App. A.1. The anomalous dimensions γ_i for the evolution of (unpolarised) PDFs are the Mellin transforms of the DGLAP splitting functions. They are given in Mellin space as functions of the complex moment variable N , conjugate to the partonic longitudinal-momentum fraction x . The splitting functions up to three loops, relevant to NNLL evolution, are computed in Refs. [72, 73].

We remark that the method developed in this paper, based on the $g^{(\gamma)}$ -functions presented above at NNLL accuracy, can be readily extended to N³LL accuracy, once the four-loop splitting functions become available: for ongoing work see Refs. [87–89], and Refs. [90–93] for studies of the associated PDF phenomenology.

A.3 g functions for TMDs

TMD evolution is encoded in the so-called Sudakov form factor S in Eq. (5.13). The computation of the factor S , leading to Eq. (5.21), can be carried out by exploiting the analytic running of the strong coupling discussed in Sec. 3, and whose perturbative ingredients are collected in App. A.1. Below, we collect all g -functions necessary to evolve TMDs up to N³LL accuracy. We also show how they are related to the $g^{(\beta)}$ -functions responsible for the evolution of α_s .

The functions g_i with $i > 0$ in Eq. (5.21) are given by

$$g_1(\lambda) = -\frac{4A^{(1)}}{a_s(\mu_0)\beta_0^2 L} \int_0^\lambda dt t g_1^{(\beta)}(t) = \frac{4A^{(1)}}{\beta_0} \frac{\lambda + \ln(1-\lambda)}{\lambda}, \quad (\text{A.6})$$

$$\begin{aligned} g_2(\lambda, \kappa) &= \int_0^\lambda dt \left[-\frac{4A^{(1)}}{\beta_0^2} t g_2^{(\beta)}(t, \kappa) - \frac{4A^{(2)}}{\beta_0^2} t (g_1^{(\beta)}(t))^2 + \frac{2\bar{B}^{(1)}}{\beta_0} g_1^{(\beta)}(t) \right] \\ &= \frac{4\beta_1 A^{(1)}}{\beta_0^3} \left(\frac{1}{2} \ln^2(1-\lambda) + \frac{\ln(1-\lambda)}{1-\lambda} + \frac{\lambda}{1-\lambda} \right) \\ &\quad - \left(\frac{4A^{(2)}}{\beta_0^2} - \frac{4A^{(1)} \ln \kappa}{\beta_0} \right) \left(\frac{\lambda}{1-\lambda} + \ln(1-\lambda) \right) - \frac{2\bar{B}^{(1)}}{\beta_0} \ln(1-\lambda), \end{aligned} \quad (\text{A.7})$$

$$\begin{aligned} g_3(\lambda, \kappa) &= -\frac{2}{\beta_0} \int_0^\lambda dt \left[\frac{2A^{(1)}}{\beta_0} t g_3^{(\beta)}(t, \kappa) + \frac{4A^{(2)}}{\beta_0} t g_1^{(\beta)}(t) g_2^{(\beta)}(t, \kappa) \right. \\ &\quad \left. + \frac{2A^{(3)}}{\beta_0} t (g_1^{(\beta)}(t))^3 - \bar{B}^{(1)} g_2^{(\beta)}(t, \kappa) - \bar{B}^{(2)} (g_1^{(\beta)}(t))^2 \right] \\ &= -\frac{4(\beta_0 \beta_2 - \beta_1^2) A^{(1)}}{\beta_0^4} \left(\frac{\lambda(3\lambda-2)}{2(1-\lambda)^2} - \ln(1-\lambda) \right) \\ &\quad + \frac{2\beta_1^2 A^{(1)}}{\beta_0^4} \left(\frac{2\lambda}{1-\lambda} + \frac{2\ln(1-\lambda)}{1-\lambda} + \frac{(1-2\lambda)\ln^2(1-\lambda)}{(1-\lambda)^2} \right) \\ &\quad + \left(\frac{4\beta_1 A^{(2)}}{\beta_0^3} - \frac{4\beta_1 A^{(1)} \ln \kappa}{\beta_0^2} \right) \left(\frac{\lambda(3\lambda-2)}{2(1-\lambda)^2} - \frac{(1-2\lambda)\ln(1-\lambda)}{(1-\lambda)^2} \right) \\ &\quad - \left(\frac{2A^{(3)}}{\beta_0^2} - \frac{4A^{(2)} \ln \kappa}{\beta_0} + 2A^{(1)} \ln^2 \kappa - \frac{2\beta_1 A^{(1)} \ln \kappa}{\beta_0^2} \right) \frac{\lambda^2}{(1-\lambda)^2} \\ &\quad - \frac{2\beta_1 \bar{B}^{(1)}}{\beta_0^2} \left(\frac{\lambda}{1-\lambda} + \frac{\ln(1-\lambda)}{1-\lambda} \right) + \left(\frac{2\bar{B}^{(2)}}{\beta_0} - 2\bar{B}^{(1)} \ln \kappa \right) \frac{\lambda}{1-\lambda}, \end{aligned} \quad (\text{A.8})$$

$$\begin{aligned}
g_4(\lambda, \kappa) &= -\frac{2}{\beta_0} \int_0^\lambda dt \left[\frac{2A^{(1)}}{\beta_0} t g_4^{(\beta)}(t, \kappa) + \frac{2A^{(2)}}{\beta_0} t \left(2g_1^{(\beta)}(t) g_3^{(\beta)}(t, \kappa) + (g_2^{(\beta)}(t, \kappa))^2 \right) \right. \\
&+ \frac{6A^{(3)}}{\beta_0} t (g_1^{(\beta)}(t))^2 g_2^{(\beta)}(t, \kappa) + \frac{2A^{(4)}}{\beta_0} t (g_1^{(\beta)}(t))^4 - \overline{B}^{(1)} g_3^{(\beta)}(t, \kappa) \\
&\left. - 2\overline{B}^{(2)} g_1^{(\beta)}(t) g_2^{(\beta)}(t, \kappa) - \overline{B}^{(3)} (g_1^{(\beta)}(t))^3 \right] \\
&= -\frac{A^{(4)}}{3(\lambda-1)^3 \beta_0^2} 2(\lambda-3)\lambda^2 \\
&+ \frac{A^{(3)}}{3(\lambda-1)^3 \beta_0^2} \left[6(\lambda-3)\lambda^2 \ln \kappa + \left(\lambda(5\lambda^2 - 15\lambda + 6) + (6 - 18\lambda) \ln(1-\lambda) \right) b_1 \right] \\
&+ \frac{A^{(2)}}{3(\lambda-1)^3 \beta_0^2} \left[\left(18\lambda^2 \beta_0^2 - 6\lambda^3 \beta_0^2 \right) \ln^2 \kappa \right. \\
&+ \left(-6b_1 \beta_0 \lambda^3 + 18b_1 \beta_0 \lambda^2 + 36 \ln(1-\lambda) b_1 \beta_0 \lambda - 12b_1 \beta_0 \lambda - 12 \ln(1-\lambda) b_1 \beta_0 \right) \ln \kappa \\
&- 11b_1^2 \lambda^3 + 8b_2 \lambda^3 + 9b_1^2 \lambda^2 + 18 \ln^2(1-\lambda) b_1^2 \lambda + 6 \ln(1-\lambda) b_1^2 \lambda - 6b_1^2 \lambda \\
&\left. - 6 \ln^2(1-\lambda) b_1^2 - 6 \ln(1-\lambda) b_1^2 \right] \\
&+ \frac{A^{(1)}}{3(\lambda-1)^3 \beta_0^2} \left[\left(2\lambda^3 \beta_0^3 - 6\lambda^2 \beta_0^3 \right) \ln^3 \kappa + \left(6\lambda b_1 \beta_0^2 - 18\lambda \ln(1-\lambda) b_1 \beta_0^2 + 6 \ln(1-\lambda) b_1 \beta_0^2 \right) \ln^2 \kappa \right. \\
&+ \left(6b_1^2 \beta_0 \lambda^3 - 6b_2 \beta_0 \lambda^3 + 6b_1^2 \beta_0 \lambda^2 - 6b_2 \beta_0 \lambda^2 - 18 \ln^2(1-\lambda) b_1^2 \beta_0 \lambda \right. \\
&+ 12 \ln(1-\lambda) b_1^2 \beta_0 \lambda + 6 \ln^2(1-\lambda) b_1^2 \beta_0 \left. \right) \ln \kappa \\
&+ 6 \ln(1-\lambda) b_1^3 \lambda^3 + 2b_1^3 \lambda^3 - 12 \ln(1-\lambda) b_1 b_2 \lambda^3 + 5b_1 b_2 \lambda^3 + 6 \ln(1-\lambda) b_3 \lambda^3 \\
&- 7b_3 \lambda^3 + 6 \ln(1-\lambda) b_1^3 \lambda^2 + 12 \ln(1-\lambda) b_1 b_2 \lambda^2 - 15b_1 b_2 \lambda^2 - 18 \ln(1-\lambda) b_3 \lambda^2 \\
&+ 15b_3 \lambda^2 - 6 \ln^3(1-\lambda) b_1^3 \lambda + 6 \ln^2(1-\lambda) b_1^3 \lambda - 18 \ln(1-\lambda) b_1 b_2 \lambda + 6b_1 b_2 \lambda \\
&\left. + 18 \ln(1-\lambda) b_3 \lambda - 6b_3 \lambda + 2 \ln^3(1-\lambda) b_1^3 + 6 \ln(1-\lambda) b_1 b_2 - 6 \ln(1-\lambda) b_3 \right] \\
&+ \frac{\overline{B}^{(3)}}{3(\lambda-1)^3 \beta_0^2} \left[-3\beta_0 \lambda^3 + 9\beta_0 \lambda^2 - 6\beta_0 \lambda \right] \\
&+ \frac{\overline{B}^{(2)}}{3(\lambda-1)^3 \beta_0^2} \left[\left(6\beta_0^2 \lambda^3 - 18\beta_0^2 \lambda^2 + 12\beta_0^2 \lambda \right) \ln \kappa \right. \\
&\left. + 3b_1 \beta_0 \lambda^3 - 9b_1 \beta_0 \lambda^2 - 6 \ln(1-\lambda) b_1 \beta_0 \lambda + 6b_1 \beta_0 \lambda + 6 \ln(1-\lambda) b_1 \beta_0 \right] \\
&+ \frac{\overline{B}^{(1)}}{3(\lambda-1)^3 \beta_0^2} \left[\left(-3\lambda^3 \beta_0^3 + 9\lambda^2 \beta_0^3 - 6\lambda \beta_0^3 \right) \ln^2 \kappa + \left(6\lambda \ln(1-\lambda) b_1 \beta_0^2 - 6 \ln(1-\lambda) b_1 \beta_0^2 \right) \ln \kappa \right. \\
&\left. - 3b_1^2 \beta_0 \lambda^3 + 3b_2 \beta_0 \lambda^3 + 3b_1^2 \beta_0 \lambda^2 - 3b_2 \beta_0 \lambda^2 + 3 \ln^2(1-\lambda) b_1^2 \beta_0 \lambda - 3 \ln^2(1-\lambda) b_1^2 \beta_0 \right], \tag{A.9}
\end{aligned}$$

with

$$\overline{B}^{(n)} = 2A^{(n)} L + B^{(n)} \quad \text{and} \quad L = \ln \frac{\kappa M}{\mu_0}, \tag{A.10}$$

(see Eq. (5.19)).

The function g_0 in Eq. (5.21) truncated at $\mathcal{O}(\alpha_s^2)$ and relevant to TMD evolution at

N³LL is given by

$$g_0(a_s(\mu_0)) = 1 - 2a_s(\mu_0) \left(A^{(1)}L^2 + B^{(1)}L \right) + \frac{1}{2}a_s^2(\mu_0) \left[4 \left(A^{(1)}L^2 + B^{(1)}L \right)^2 + \frac{2}{3} \left(-2A^{(1)}\beta_0L^3 + 6A^{(1)}\beta_0L^2 \ln \kappa - 6A^{(2)}L^2 - 3\beta_0B^{(1)}L^2 + 6\beta_0B^{(1)}L \ln \kappa - 6B^{(2)}L \right) \right]. \quad (\text{A.11})$$

As discussed in Sec. 5.2, the coefficients $A^{(n)}$ and $B^{(n)}$ are related to the anomalous dimensions γ_K , γ_F , and K that govern the evolution of TMDs (see Eqs. (5.1) and (5.5)). In Eq. (5.15), we have derived these relationships up to N³LL accuracy. Below, we report the perturbative coefficients of the TMD anomalous dimensions necessary to reconstruct the coefficients $A^{(n)}$ and $B^{(n)}$ in the quark case up to N³LL accuracy [94–96]. For the cusp anomalous dimension γ_K we have

$$\begin{aligned} \gamma_K^{(0)} &= 8C_F, \\ \gamma_K^{(1)} &= 8C_F \left[\left(\frac{67}{9} - \frac{\pi^2}{3} \right) C_A - \frac{20}{9} T_R n_f \right], \\ \gamma_K^{(2)} &= 8C_F \left[\left(\frac{245}{6} - \frac{134\pi^2}{27} + \frac{11\pi^4}{45} + \frac{22\zeta_3}{3} \right) C_A^2 + \left(-\frac{418}{27} + \frac{40\pi^2}{27} - \frac{56\zeta_3}{3} \right) C_A T_R n_f + \left(-\frac{55}{3} + 16\zeta_3 \right) C_F T_R n_f - \frac{16}{27} n_f^2 T_R^2 \right], \\ \gamma_K^{(3)} &= 2C_F \left[n_f^3 \left(\frac{64\zeta_3}{27} - \frac{32}{81} \right) + n_f^2 C_A \left(-\frac{224\zeta_2^2}{15} + \frac{2240\zeta_3}{27} - \frac{608\zeta_2}{81} + \frac{923}{81} \right) + n_f^2 C_F \left(\frac{64\zeta_2^2}{5} - \frac{640\zeta_3}{9} + \frac{2392}{81} \right) + n_f C_A^2 \left(\frac{2096\zeta_5}{9} + \frac{448\zeta_3\zeta_2}{3} - \frac{352\zeta_2^2}{15} - \frac{23104\zeta_3}{27} + \frac{20320\zeta_2}{81} - \frac{24137}{81} \right) + n_f C_A C_F \left(160\zeta_5 - 128\zeta_3\zeta_2 - \frac{352\zeta_2^2}{5} + \frac{3712\zeta_3}{9} + \frac{440\zeta_2}{3} - \frac{34066}{81} \right) + n_f C_F^2 \left(-320\zeta_5 + \frac{592\zeta_3}{3} + \frac{572}{9} \right) + n_f d_F^{abcd} d_F^{abcd} \left(-\frac{1}{3} (1280\zeta_5) - \frac{256\zeta_3}{3} + 256\zeta_2 \right) + d_A^{abcd} d_F^{abcd} \left(-384\zeta_3^2 - \frac{7936\zeta_2^3}{35} + \frac{3520\zeta_5}{3} + \frac{128\zeta_3}{3} - 128\zeta_2 \right) + C_A^3 \left(-16\zeta_3^2 - \frac{20032\zeta_2^3}{105} - \frac{3608\zeta_5}{9} - \frac{352\zeta_3\zeta_2}{3} + \frac{3608\zeta_2^2}{5} + \frac{20944\zeta_3}{27} - \frac{88400\zeta_2}{81} + \frac{84278}{81} \right) \right]. \quad (\text{A.12}) \end{aligned}$$

For the anomalous dimension γ_F we have

$$\begin{aligned}
\gamma_F^{(0)} &= 6C_F, \\
\gamma_F^{(1)} &= - \left[C_F^2 \left(-3 + 4\pi^2 - 48\zeta_3 \right) + C_F C_A \left(-\frac{961}{27} - \frac{11\pi^2}{3} + 52\zeta_3 \right) + C_F T_R n_f \left(\frac{260}{27} + \frac{4\pi^2}{3} \right) \right], \\
\gamma_F^{(2)} &= - \left[C_F^3 \left(-29 - 6\pi^2 - \frac{16\pi^4}{5} - 136\zeta_3 + \frac{32\pi^2\zeta_3}{3} + 480\zeta_5 \right) \right. \\
&\quad + C_F^2 C_A \left(-\frac{151}{2} + \frac{410\pi^2}{9} + \frac{494\pi^4}{135} - \frac{1688\zeta_3}{3} - \frac{16\pi^2\zeta_3}{3} - 240\zeta_5 \right) \\
&\quad + C_F C_A^2 \left(-\frac{139345}{1458} - \frac{7163\pi^2}{243} - \frac{83\pi^4}{45} + \frac{7052\zeta_3}{9} - \frac{88\pi^2\zeta_3}{9} - 272\zeta_5 \right) \\
&\quad + C_F^2 T_R n_f \left(\frac{5906}{27} - \frac{52\pi^2}{9} - \frac{56\pi^4}{27} + \frac{1024\zeta_3}{9} \right) \\
&\quad + C_F C_A T_R n_f \left(-\frac{34636}{729} + \frac{5188\pi^2}{243} + \frac{44\pi^4}{45} - \frac{3856\zeta_3}{27} \right) \\
&\quad \left. + C_F T_R^2 n_f^2 \left(\frac{19336}{729} - \frac{80\pi^2}{27} - \frac{64\zeta_3}{27} \right) \right]. \tag{A.13}
\end{aligned}$$

For the anomalous dimension K we have

$$\begin{aligned}
K^{(0)} &= 0, \\
K^{(1)} &= C_F \left[C_A \left(28\zeta_3 - \frac{808}{27} \right) + \frac{224 T_R n_f}{27} \right], \\
K^{(2)} &= 2C_F \left[\frac{1}{2} C_A^2 \left(-\frac{176}{3} \zeta_3 \zeta_2 + \frac{6392\zeta_2}{81} + \frac{12328\zeta_3}{27} + \frac{154\zeta_4}{3} - 192\zeta_5 - \frac{297029}{729} \right) \right. \\
&\quad + C_A T_R n_f \left(-\frac{824}{81} \zeta_2 - \frac{904\zeta_3}{27} + \frac{20\zeta_4}{3} + \frac{62626}{729} \right) \\
&\quad \left. + 2T_R^2 n_f^2 \left(-\frac{32}{9} \zeta_3 - \frac{1856}{729} \right) + C_F T_R n_f \left(-\frac{304}{9} \zeta_3 - 16\zeta_4 + \frac{1711}{27} \right) \right]. \tag{A.14}
\end{aligned}$$

By plugging the coefficients in Eqs. (A.12), (A.13), and (A.14) into Eq. (5.15), we have checked that we find agreement with the perturbative coefficients of the functions A and B as implemented in the DYTURBO code [49].

References

- [1] V. Bertone, G. Bozzi and F. Hautmann, *Perturbative hysteresis and emergent resummation scales*, *Phys. Rev. D* **105** (2022) 096003 [2202.03380].
- [2] V.N. Gribov and L.N. Lipatov, *Deep inelastic $e p$ scattering in perturbation theory*, *Sov. J. Nucl. Phys.* **15** (1972) 438.
- [3] G. Altarelli and G. Parisi, *Asymptotic Freedom in Parton Language*, *Nucl. Phys. B* **126** (1977) 298.
- [4] Y.L. Dokshitzer, *Calculation of the Structure Functions for Deep Inelastic Scattering and $e+e-$ Annihilation by Perturbation Theory in Quantum Chromodynamics.*, *Sov. Phys. JETP* **46** (1977) 641.
- [5] PDF4LHC WORKING GROUP collaboration, *The PDF4LHC21 combination of global PDF fits for the LHC Run III*, *J. Phys. G* **49** (2022) 080501 [2203.05506].

- [6] NNPDF collaboration, *The path to proton structure at 1% accuracy*, *Eur. Phys. J. C* **82** (2022) 428 [2109.02653].
- [7] NNPDF collaboration, *Parton Distributions with Theory Uncertainties: General Formalism and First Phenomenological Studies*, *Eur. Phys. J. C* **79** (2019) 931 [1906.10698].
- [8] S. Bailey, T. Cridge, L.A. Harland-Lang, A.D. Martin and R.S. Thorne, *Parton distributions from LHC, HERA, Tevatron and fixed target data: MSHT20 PDFs*, *Eur. Phys. J. C* **81** (2021) 341 [2012.04684].
- [9] T.-J. Hou et al., *New CTEQ global analysis of quantum chromodynamics with high-precision data from the LHC*, *Phys. Rev. D* **103** (2021) 014013 [1912.10053].
- [10] S. Alekhin, J. Blümlein, S. Moch and R. Placakyte, *Parton distribution functions, α_s , and heavy-quark masses for LHC Run II*, *Phys. Rev. D* **96** (2017) 014011 [1701.05838].
- [11] H1, ZEUS collaboration, *Combination of measurements of inclusive deep inelastic $e^\pm p$ scattering cross sections and QCD analysis of HERA data*, *Eur. Phys. J. C* **75** (2015) 580 [1506.06042].
- [12] P. Azzi et al., *Report from Working Group 1: Standard Model Physics at the HL-LHC and HE-LHC*, *CERN Yellow Rep. Monogr.* **7** (2019) 1 [1902.04070].
- [13] LHeC, FCC-HE STUDY GROUP collaboration, *The Large Hadron–Electron Collider at the HL-LHC*, *J. Phys. G* **48** (2021) 110501 [2007.14491].
- [14] FCC collaboration, *FCC Physics Opportunities: Future Circular Collider Conceptual Design Report Volume 1*, *Eur. Phys. J. C* **79** (2019) 474.
- [15] Y. Hatta et al., *Proceedings, Probing Nucleons and Nuclei in High Energy Collisions: Dedicated to the Physics of the Electron Ion Collider: Seattle (WA), United States, October 1 - November 16, 2018*, **2002.12333**.
- [16] V. Bertone, G. Bozzi and F. Hautmann, *Resummation Scales and the Assessment of Theoretical Uncertainties in Parton Distribution Functions*, in *29th International Workshop on Deep-Inelastic Scattering and Related Subjects*, 5, 2022 [2205.15900].
- [17] V. Bertone, G. Bozzi and F. Hautmann, *Structure functions and perturbative hysteresis*, *PoS EPS-HEP2023* (2024) 256.
- [18] T. Jaroszewicz, *Gluonic Regge Singularities and Anomalous Dimensions in QCD*, *Phys. Lett. B* **116** (1982) 291.
- [19] S. Catani and F. Hautmann, *Quark anomalous dimensions at small x* , *Phys. Lett. B* **315** (1993) 157.
- [20] S. Catani and F. Hautmann, *High-energy factorization and small x deep inelastic scattering beyond leading order*, *Nucl. Phys. B* **427** (1994) 475 [hep-ph/9405388].
- [21] J. Kwiecinski, *The Gluon Distributions in the Small x Region Beyond the Leading Order*, *Z. Phys. C* **29** (1985) 561.
- [22] R.K. Ellis, Z. Kunszt and E.M. Levin, *The Evolution of parton distributions at small x* , *Nucl. Phys. B* **420** (1994) 517.
- [23] R.K. Ellis, F. Hautmann and B.R. Webber, *QCD scaling violation at small x* , *Phys. Lett. B* **348** (1995) 582 [hep-ph/9501307].
- [24] J.R. Forshaw, R.G. Roberts and R.S. Thorne, *Analytic approach to small x structure functions*, *Phys. Lett. B* **356** (1995) 79 [hep-ph/9504336].

- [25] R.D. Ball and S. Forte, *Summation of leading logarithms at small x* , *Phys. Lett. B* **351** (1995) 313 [[hep-ph/9501231](#)].
- [26] J. Kwiecinski, A.D. Martin and A.M. Stasto, *A Unified BFKL and GLAP description of F_2 data*, *Phys. Rev. D* **56** (1997) 3991 [[hep-ph/9703445](#)].
- [27] M. Ciafaloni, D. Colferai, G.P. Salam and A.M. Stasto, *A Matrix formulation for small- x singlet evolution*, *JHEP* **08** (2007) 046 [[0707.1453](#)].
- [28] G. Altarelli, R.D. Ball and S. Forte, *Small x Resummation with Quarks: Deep-Inelastic Scattering*, *Nucl. Phys. B* **799** (2008) 199 [[0802.0032](#)].
- [29] C.D. White and R.S. Thorne, *A Global Fit to Scattering Data with NLL BFKL Resummations*, *Phys. Rev. D* **75** (2007) 034005 [[hep-ph/0611204](#)].
- [30] R.D. Ball, V. Bertone, M. Bonvini, S. Marzani, J. Rojo and L. Rottoli, *Parton distributions with small- x resummation: evidence for BFKL dynamics in HERA data*, *Eur. Phys. J. C* **78** (2018) 321 [[1710.05935](#)].
- [31] xFITTER DEVELOPERS' TEAM collaboration, *Impact of low- x resummation on QCD analysis of HERA data*, *Eur. Phys. J. C* **78** (2018) 621 [[1802.00064](#)].
- [32] M.A. Ebert, *Analytic results for Sudakov form factors in QCD*, *JHEP* **02** (2022) 136 [[2110.11360](#)].
- [33] G. Billis, F.J. Tackmann and J. Talbert, *Higher-Order Sudakov Resummation in Coupled Gauge Theories*, *JHEP* **03** (2020) 182 [[1907.02971](#)].
- [34] F. Hautmann, L. Keersmaekers, A. Lelek and A.M. Van Kampen, *Dynamical resolution scale in transverse momentum distributions at the LHC*, *Nucl. Phys. B* **949** (2019) 114795 [[1908.08524](#)].
- [35] J.C. Collins, D.E. Soper and G.F. Sterman, *Transverse Momentum Distribution in Drell-Yan Pair and W and Z Boson Production*, *Nucl. Phys. B* **250** (1985) 199.
- [36] J. Collins, *Foundations of Perturbative QCD*, vol. 32 of *Cambridge Monographs on Particle Physics, Nuclear Physics and Cosmology*, Cambridge University Press (7, 2023), [10.1017/9781009401845](#).
- [37] R. Angeles-Martinez et al., *Transverse Momentum Dependent (TMD) parton distribution functions: status and prospects*, *Acta Phys. Polon. B* **46** (2015) 2501 [[1507.05267](#)].
- [38] R. Boussarie et al., *TMD Handbook*, [2304.03302](#).
- [39] R. Abdul Khalek et al., *Snowmass 2021 White Paper: Electron Ion Collider for High Energy Physics*, [2203.13199](#).
- [40] I. Scimemi and A. Vladimirov, *Non-perturbative structure of semi-inclusive deep-inelastic and Drell-Yan scattering at small transverse momentum*, *JHEP* **06** (2020) 137 [[1912.06532](#)].
- [41] A. Bacchetta, V. Bertone, C. Bissolotti, G. Bozzi, F. Delcarro, F. Piacenza et al., *Transverse-momentum-dependent parton distributions up to N^3LL from Drell-Yan data*, *JHEP* **07** (2020) 117 [[1912.07550](#)].
- [42] F. Hautmann, I. Scimemi and A. Vladimirov, *Non-perturbative contributions to vector-boson transverse momentum spectra in hadronic collisions*, *Phys. Lett. B* **806** (2020) 135478 [[2002.12810](#)].

- [43] MAP (MULTI-DIMENSIONAL ANALYSES OF PARTONIC DISTRIBUTIONS) collaboration, *Unpolarized transverse momentum distributions from a global fit of Drell-Yan and semi-inclusive deep-inelastic scattering data*, *JHEP* **10** (2022) 127 [[2206.07598](#)].
- [44] M. Bury, F. Hautmann, S. Leal-Gomez, I. Scimemi, A. Vladimirov and P. Zurita, *PDF bias and flavor dependence in TMD distributions*, *JHEP* **10** (2022) 118 [[2201.07114](#)].
- [45] V. Moos, I. Scimemi, A. Vladimirov and P. Zurita, *Extraction of unpolarized transverse momentum distributions from the fit of Drell-Yan data at N^4LL* , *JHEP* **05** (2024) 036 [[2305.07473](#)].
- [46] MAP collaboration, *Flavor dependence of unpolarized quark Transverse Momentum Distributions from a global fit*, [2405.13833](#).
- [47] CDF collaboration, *High-precision measurement of the W boson mass with the CDF II detector*, *Science* **376** (2022) 170.
- [48] ATLAS collaboration, *Measurement of the W -boson mass and width with the ATLAS detector using proton-proton collisions at $\sqrt{s} = 7$ TeV*, [2403.15085](#).
- [49] S. Camarda et al., *DYTurbo: Fast predictions for Drell-Yan processes*, *Eur. Phys. J. C* **80** (2020) 251 [[1910.07049](#)].
- [50] S. Camarda, L. Cieri and G. Ferrera, *Drell-Yan lepton-pair production: q_T resummation at N^3LL accuracy and fiducial cross sections at N^3LO* , *Phys. Rev. D* **104** (2021) L111503 [[2103.04974](#)].
- [51] S. Camarda, G. Ferrera and M. Schott, *Determination of the strong-coupling constant from the Z -boson transverse-momentum distribution*, *Eur. Phys. J. C* **84** (2024) 39 [[2203.05394](#)].
- [52] S. Camarda, L. Cieri and G. Ferrera, *Drell-Yan lepton-pair production: q_T resummation at N_4LL accuracy*, *Phys. Lett. B* **845** (2023) 138125 [[2303.12781](#)].
- [53] W. Bizoń, X. Chen, A. Gehrmann-De Ridder, T. Gehrmann, N. Glover, A. Huss et al., *Fiducial distributions in Higgs and Drell-Yan production at $N^3LL+NNLO$* , *JHEP* **12** (2018) 132 [[1805.05916](#)].
- [54] W. Bizon, A. Gehrmann-De Ridder, T. Gehrmann, N. Glover, A. Huss, P.F. Monni et al., *The transverse momentum spectrum of weak gauge bosons at $N^3LL + NNLO$* , *Eur. Phys. J. C* **79** (2019) 868 [[1905.05171](#)].
- [55] X. Chen, T. Gehrmann, E.W.N. Glover, A. Huss, P.F. Monni, E. Re et al., *Third-Order Fiducial Predictions for Drell-Yan Production at the LHC*, *Phys. Rev. Lett.* **128** (2022) 252001 [[2203.01565](#)].
- [56] A. Bermudez Martinez et al., *Production of Z -bosons in the parton branching method*, *Phys. Rev. D* **100** (2019) 074027 [[1906.00919](#)].
- [57] A. Bermudez Martinez, F. Hautmann and M.L. Mangano, *TMD evolution and multi-jet merging*, *Phys. Lett. B* **822** (2021) 136700 [[2107.01224](#)].
- [58] A. Bermudez Martinez, F. Hautmann and M.L. Mangano, *Multi-jet merging with TMD parton branching*, *JHEP* **09** (2022) 060 [[2208.02276](#)].
- [59] I. Bujanja et al., *The small k_T region in Drell-Yan production at next-to-leading order with the parton branching method*, *Eur. Phys. J. C* **84** (2024) 154 [[2312.08655](#)].
- [60] J. Isaacson, Y. Fu and C.P. Yuan, *Improving ResBos for the precision needs of the LHC*, [2311.09916](#).

- [61] T. Becher and T. Neumann, *Fiducial q_T resummation of color-singlet processes at $N^3LL+NNLO$* , *JHEP* **03** (2021) 199 [[2009.11437](#)].
- [62] T. Neumann and J. Campbell, *Fiducial Drell-Yan production at the LHC improved by transverse-momentum resummation at N^4LLp+N^3LO* , *Phys. Rev. D* **107** (2023) L011506 [[2207.07056](#)].
- [63] J. Campbell and T. Neumann, *Third order QCD predictions for fiducial W-boson production*, *JHEP* **11** (2023) 127 [[2308.15382](#)].
- [64] M.A. Ebert and F.J. Tackmann, *Resummation of Transverse Momentum Distributions in Distribution Space*, *JHEP* **02** (2017) 110 [[1611.08610](#)].
- [65] M.A. Ebert, J.K.L. Michel, I.W. Stewart and F.J. Tackmann, *Drell-Yan q_T resummation of fiducial power corrections at N^3LL* , *JHEP* **04** (2021) 102 [[2006.11382](#)].
- [66] S. Catani, M.L. Mangano, P. Nason and L. Trentadue, *The Resummation of soft gluons in hadronic collisions*, *Nucl. Phys. B* **478** (1996) 273 [[hep-ph/9604351](#)].
- [67] S. Catani, D. de Florian, M. Grazzini and P. Nason, *Soft gluon resummation for Higgs boson production at hadron colliders*, *JHEP* **07** (2003) 028 [[hep-ph/0306211](#)].
- [68] G. Bozzi, S. Catani, D. de Florian and M. Grazzini, *Transverse-momentum resummation and the spectrum of the Higgs boson at the LHC*, *Nucl. Phys. B* **737** (2006) 73 [[hep-ph/0508068](#)].
- [69] R.K. Ellis, W.J. Stirling and B.R. Webber, *QCD and collider physics*, vol. 8, Cambridge University Press (2, 2011), [10.1017/CBO9780511628788](#).
- [70] G. Curci, W. Furmanski and R. Petronzio, *Evolution of Parton Densities Beyond Leading Order: The Nonsinglet Case*, *Nucl. Phys. B* **175** (1980) 27.
- [71] W. Furmanski and R. Petronzio, *Singlet Parton Densities Beyond Leading Order*, *Phys. Lett. B* **97** (1980) 437.
- [72] S. Moch, J.A.M. Vermaseren and A. Vogt, *The Three loop splitting functions in QCD: The Nonsinglet case*, *Nucl. Phys. B* **688** (2004) 101 [[hep-ph/0403192](#)].
- [73] A. Vogt, S. Moch and J.A.M. Vermaseren, *The Three-loop splitting functions in QCD: The Singlet case*, *Nucl. Phys. B* **691** (2004) 129 [[hep-ph/0404111](#)].
- [74] M. Dittmar et al., *Working Group I: Parton distributions: Summary report for the HERA LHC Workshop Proceedings*, [hep-ph/0511119](#).
- [75] V. Bertone, S. Carrazza and E.R. Nocera, *Reference results for time-like evolution up to $\mathcal{O}(\alpha_s^3)$* , *JHEP* **03** (2015) 046 [[1501.00494](#)].
- [76] T. Becher and M. Neubert, *Drell-Yan Production at Small q_T , Transverse Parton Distributions and the Collinear Anomaly*, *Eur. Phys. J. C* **71** (2011) 1665 [[1007.4005](#)].
- [77] S. Catani, D. de Florian, G. Ferrera and M. Grazzini, *Vector boson production at hadron colliders: transverse-momentum resummation and leptonic decay*, *JHEP* **12** (2015) 047 [[1507.06937](#)].
- [78] PARTICLE DATA GROUP collaboration, *Review of Particle Physics*, *PTEP* **2020** (2020) 083C01.
- [79] V. Bertone, S. Carrazza and J. Rojo, *APFEL: A PDF Evolution Library with QED corrections*, *Comput. Phys. Commun.* **185** (2014) 1647 [[1310.1394](#)].

- [80] V. Bertone, *APFEL++: A new PDF evolution library in C++*, *PoS DIS2017* (2018) 201 [[1708.00911](#)].
- [81] R.J. Gonsalves, J. Pawłowski and C.-F. Wai, *QCD Radiative Corrections to Electroweak Boson Production at Large Transverse Momentum in Hadron Collisions*, *Phys. Rev. D* **40** (1989) 2245.
- [82] A. Buckley, J. Ferrando, S. Lloyd, K. Nordström, B. Page, M. Rüfenacht et al., *LHAPDF6: parton density access in the LHC precision era*, *Eur. Phys. J. C* **75** (2015) 132 [[1412.7420](#)].
- [83] G.P. Salam and J. Rojo, *A Higher Order Perturbative Parton Evolution Toolkit (HOPPET)*, *Comput. Phys. Commun.* **180** (2009) 120 [[0804.3755](#)].
- [84] V. Bertone and A. Karlberg, *Benchmark of deep-inelastic-scattering structure functions at $\mathcal{O}(\alpha_s^3)$* , [2404.15711](#).
- [85] F. Herzog, B. Ruijl, T. Ueda, J.A.M. Vermaseren and A. Vogt, *The five-loop beta function of Yang-Mills theory with fermions*, *JHEP* **02** (2017) 090 [[1701.01404](#)].
- [86] T. Rowland and E.W. Weisstein, “Matrix exponential. from mathworld—a wolfram web resource. From MathWorld—A Wolfram Web Resource.”
- [87] S. Moch, B. Ruijl, T. Ueda, J. Vermaseren and A. Vogt, *Additional moments and x -space approximations of four-loop splitting functions in QCD*, *Phys. Lett. B* **849** (2024) 138468 [[2310.05744](#)].
- [88] G. Falcioni, F. Herzog, S. Moch and A. Vogt, *Four-loop splitting functions in QCD – The gluon-to-quark case*, *Phys. Lett. B* **846** (2023) 138215 [[2307.04158](#)].
- [89] G. Falcioni, F. Herzog, S. Moch and A. Vogt, *Four-loop splitting functions in QCD – The quark-quark case*, *Phys. Lett. B* **842** (2023) 137944 [[2302.07593](#)].
- [90] J. McGowan, T. Cridge, L.A. Harland-Lang and R.S. Thorne, *Approximate N^3 LO parton distribution functions with theoretical uncertainties: MSHT20a N^3 LO PDFs*, *Eur. Phys. J. C* **83** (2023) 185 [[2207.04739](#)].
- [91] T. Cridge, L.A. Harland-Lang and R.S. Thorne, *Combining QED and Approximate N^3 LO QCD Corrections in a Global PDF Fit: MSHT20qed_an3lo PDFs*, [2312.07665](#).
- [92] T. Cridge, L.A. Harland-Lang and R.S. Thorne, *The Impact of LHC Jet and Z_{pT} Data at up to Approximate N^3 LO Order in the MSHT Global PDF Fit*, [2312.12505](#).
- [93] NNPDF collaboration, *The Path to N^3 LO Parton Distributions*, [2402.18635](#).
- [94] J. Collins and T.C. Rogers, *Connecting Different TMD Factorization Formalisms in QCD*, *Phys. Rev. D* **96** (2017) 054011 [[1705.07167](#)].
- [95] J.M. Henn, G.P. Korchemsky and B. Mistlberger, *The full four-loop cusp anomalous dimension in $\mathcal{N} = 4$ super Yang-Mills and QCD*, *JHEP* **04** (2020) 018 [[1911.10174](#)].
- [96] A. von Manteuffel, E. Panzer and R.M. Schabinger, *Cusp and collinear anomalous dimensions in four-loop QCD from form factors*, *Phys. Rev. Lett.* **124** (2020) 162001 [[2002.04617](#)].